

Investigating the impact of modeling assumptions and closure models on the steady-state prediction of solar-driven methane steam reforming in a porous reactor

Jorge E.P. Navalho^{a,b,*}, José C.F. Pereira^b

^a Departamento de Engenharia Mecânica e Industrial, Faculdade de Ciências e Tecnologia, Universidade Nova de Lisboa, 2829-516 Caparica, Portugal

^b LAETA, IDMEC, Instituto Superior Técnico, Universidade de Lisboa, Av. Rovisco Pais, 1, 1049-001 Lisbon, Portugal

ARTICLE INFO

Keywords:

Concentrated solar energy
Solar thermochemical reactor
Methane steam reforming
Open-cell ceramic foam
Modeling assumptions
Closure models

ABSTRACT

In this work, the effect of different modeling assumptions and closure models — frequently considered in the literature of solar thermochemical reactors and closely-related areas — is investigated. The application of different modeling assumptions and closure models may strongly affect the results accuracy and compromise a meaningful comparison across literature works. The following is herein investigated: (i) the role of upstream and downstream fluid regions to the two-phase reactor region; (ii) relevance of species and gas-phase thermal diffusion mechanisms; (iii) reaction heat accounted for in gas- or solid-phase energy balance equations; (iv) local thermal equilibrium (LTE) vs. local thermal non-equilibrium (LTNE) models; (v) model dimension (one-dimensional vs. two-dimensional axisymmetric models); (vi) local volumetric convection heat transfer correlations; and (vii) effective solid thermal conductivity correlations. The relevance of this work extends well beyond the current application (methane steam reforming in a volumetric solar reactor), since similar models and assumptions have also been widely applied for predicting the performance of volumetric solar absorbers and dry reforming solar reactors. The results show that an upstream fluid region should be considered while applying inlet first-type boundary conditions and diffusion transport in the corresponding governing equations to ensure full-conservation and simultaneously to account for developing profiles upstream the reactor inlet section. For the operating conditions considered, species diffusion and gas-phase heat conduction are particularly relevant at the reactor centerline but with a negligible integral effect. A significant difference in the reactor performance is observed while accounting for the reaction heat from surface reactions in the solid- or gas-phase energy balances — for the lowest inlet gas velocity herein considered, the thermochemical efficiency (methane conversion) is approximately equal to 70.8% (76.3%) and 77.3% (84.7%) assigning the reaction heat to the gas- and solid-phase energy balances, respectively. LTE model results are strikingly different from the results obtained with the LTNE model considering the reaction heat accounted for in the gas-phase energy balance but not significantly different from the results computed with the LTNE model with the reaction heat assigned to the solid-phase energy balance. One-dimensional reactor modeling provided with an average concentrated solar heat flux value results in a similar average performance as that given by a two-dimensional model but fails to predict the high temperatures observed at reactor centerline — for the lowest inlet gas velocity, the difference between the maximum solid temperatures predicted by one- and two-dimensional models is about 340 K.

1. Introduction

Much progress has been made in the field of concentrated solar energy applications that make use of volumetric (porous) structures for producing high-temperature heat (volumetric solar absorbers) and for promoting highly endothermic chemical reactions (volumetric solar thermochemical reactors). This progress has been greatly benefited

from the application of advanced and highly reliable models and numerical simulation techniques (numerical studies) [1–3]. Although the interest in developing volumetric solar collector systems emerged in late 70's–early 80's of last century [4,5] — as generally the interest in concentrated solar power due to the 1970's oil crisis [6] —, it was

* Corresponding author at: Departamento de Engenharia Mecânica e Industrial, Faculdade de Ciências e Tecnologia, Universidade Nova de Lisboa, 2829-516 Caparica, Portugal.

E-mail addresses: jorge.navalho@fct.unl.pt (J.E.P. Navalho), jcfcpereira@tecnico.ulisboa.pt (J.C.F. Pereira).

<https://doi.org/10.1016/j.enconman.2023.117577>

Received 10 June 2023; Received in revised form 12 August 2023; Accepted 23 August 2023

Available online 9 September 2023

0196-8904/© 2023 The Author(s). Published by Elsevier Ltd. This is an open access article under the CC BY license (<http://creativecommons.org/licenses/by/4.0/>).

Nomenclature

A	Area, m ²
a_v	Specific surface area, m ⁻¹
c_p	Specific heat, J kg ⁻¹ K ⁻¹
D_k^T	Thermal diffusion coefficient for species k , kg m ⁻¹ s ⁻¹
D_{kj}	Binary diffusion coefficient, m ² s ⁻¹
D_{km}	Mixture-average diffusion coefficient for species k , m ² s ⁻¹
d_c	Porous foam mean cell diameter, m
d_p	Porous foam mean pore diameter, m
$F_{cat/geo}$	Ratio of catalytic surface area to geometric surface area, –
G_c	Collimated (incident) solar irradiation, W m ⁻²
G_d	Diffusive irradiation, W m ⁻²
h	Specific enthalpy, J kg ⁻¹ ; convection heat transfer coefficient, W m ⁻² K ⁻¹
h_v	Volumetric convection heat transf. coef., W m ⁻³ K ⁻¹
J_k	Diffusive mass flux of species k , kg m ⁻² s ⁻¹
K	Total number of chemical species, –
\dot{m}	Mass flow rate, kg s ⁻¹
Pr	Prandtl number, –
p	Pressure, Pa
Q_0	Total concentrated solar power provided to the reactor, W
q_0''	Concentrated solar heat flux at the reactor front section, W m ⁻²
q_r	Radiative heat flux, W m ⁻²
R	Ideal gas constant, J kmol ⁻¹ K ⁻¹
Re	Local Reynolds number, –
r	Transversal (radial) coordinate, m
S	Selectivity, –
\dot{s}_k	Production rate of species k , kmol m ⁻² s ⁻¹
T	Temperature, K
T_∞	Surrounding surfaces and fluid temperature, K
t	Time, s
U	Overall heat transfer coefficient, W m ⁻² K ⁻¹
u	Axial component of superficial gas velocity, m s ⁻¹
\mathbf{u}	Superficial gas velocity, m s ⁻¹
V_{react}	Total reactor volume, m ³
v	Radial component of superficial gas velocity, m s ⁻¹
\overline{W}	Mean (mixture) molar weight, kg kmol ⁻¹
W_k	Molar weight of species k , kg kmol ⁻¹
X_k	Mole fraction of species k , –
x	Longitudinal (axial) coordinate, m
Y_k	Mass fraction of species k , –
Greek symbols	
β	Extinction coefficient, m ⁻¹
Δp	Pressure drop along the reactor, Pa

ϵ	Emissivity, –
η_{chem}	Chemical efficiency, –
η_{th}	Thermochemical efficiency, –
κ	Absorption coefficient, m ⁻¹
λ	Thermal conductivity, W m ⁻¹ K ⁻¹
μ	Dynamic viscosity, Pa s ⁻¹
ρ	Density, kg m ⁻³
σ	Stefan–Boltzmann constant, W m ⁻² K ⁻⁴
σ_s	Scattering coefficient, m ⁻¹
ϕ	Foam porosity, –
χ_k	Conversion of reactant species k –
$\dot{\omega}_k$	Volumetric production rate of species k , kmol m ⁻³ s ⁻¹

Subscripts

avg	Average
eff	Effective
equil	Equilibrium state
front	Reactor front (irradiated) section
g	Gas mixture; gas-phase
in	Inlet section; initial state
k	Species k
out	Outlet section
react	Reactor
s	Solid-phase
w	Wall

only from research centers and companies historically committed to the subject — as during the previous decades, with few exceptions — but mainly from different and worldwide research groups with disparate backgrounds and research interests which reveals a widespread engagement of the scientific community on the topic. This engagement has been driven by a general societal trend towards a decarbonized energy economy combined with the large availability of multi-disciplinary, general-purpose, and user-friendly simulation software tools that allow to accurately predict the operation of solar collectors. Even though most of the contributions to this field are based on numerical studies, little attention has been paid to the underlying modeling assumptions and required closure models — models applied to close the system of governing equations. Modeling assumptions and closure models may affect the accuracy of numerical predictions and lead to inconsistent and conflicting conclusions among different works.

Volumetric solar thermochemical reactors have been extensively investigated for synthesis gas and hydrogen production through catalytic reforming (steam, dry and bi-reforming) [9–11] and redox cycles [12, 13]. For open-cell foam reforming reactors (and volumetric solar absorbers), much attention has been devoted to the following: (i) the medium pore structure features (porosity and cell/pore diameter) considering a single uniform structure [9,14–16] and combinations of different uniform structures [11,16–18]; (ii) the effect of material (thermophysical) properties — solid-phase intrinsic thermal conductivity and surface emissivity [15,19,20]; and (iii) operating conditions — feed mixture composition, temperature, and inlet gas velocity, and concentrated solar flux distribution [14,15,18]. Enhancement of the reactor performance by reducing heat losses and increasing the thermal-to-chemical energy conversion has been the main motivation for these works. With the same concern in mind (performance improvement), other works have suggested reactor designs different than the conventional tubular single-pass reactor [21–23].

mainly in the 1990's that the first numerical studies were reported — see e.g. Refs. [7,8]. Particularly, during the last decade a very large (unprecedented) number of numerical works has been reported not

Due to the typical tubular (cylindrical) foam structure geometry for the reactor/receiver and operation symmetry along the tangential (circumferential) direction, two-dimensional (2D) axisymmetric volume-averaging models have been largely preferred. Numerical predictions applying the volume-averaging — continuum, continuous-scale, homogeneous equivalent, or porous medium — approach with suitable closure models and modeling assumptions are known to agree fairly well with experimental results. (Pore-scale (direct) numerical simulations, particularly, on the performance of open-cell foam solar applications are scarcely found in the literature [24,25] but are extremely relevant for detailed fluid flow and heat transfer performance investigations in porous media, as well as for the development of hydrodynamic and heat transfer correlations (closure models for the volume-averaging approach) to estimate local and effective medium properties [26–29].) Nevertheless, there are many underlying modeling assumptions and closure models that differ among works applying the volume-averaging method on this topic. Different correlations to compute convection heat transfer coefficients, effective solid thermal conductivities, and radiative properties have been considered. (Particularly, for volumetric solar absorbers, several works discuss the results obtained with different correlations to compute convection heat transfer coefficients [14,30–33] — even though some of such correlations were developed for different hydrothermal conditions, geometrical parameters, and porous media (packed bed, open-cell foams, wire meshes, and honeycomb monoliths) — and radiative properties [33,34]). Different radiative heat transfer models have been applied and compared [34–37]. One-dimensional (1D) models have been considered to decrease the overall model complexity — see Refs. [34,38,39] and Ref. [40] for volumetric solar absorbers and solar thermochemical reactors, respectively. Single- and two-phase energy models have also been applied — local thermal equilibrium (LTE) [41–44] and local thermal non-equilibrium (LTNE) [14,18,45] approaches, respectively —, even though it is largely accepted, particularly for the performance prediction of volumetric solar absorbers, that LTE models should be avoided because these models may lead to a significantly different operation [34]. Concerning the heat conduction in the solid phase, two different correlations (differing by a factor of 1/3) have been applied for computing the effective solid thermal conductivity of open-cell foams — see Refs. [15,34,46]. As far as the authors are aware, the effects of model dimension (1D vs. 2D axisymmetric models), external heat transfer resistance (negligible (LTE model) vs. finite (LTNE model)), and correlations for external (convection) heat transfer coefficient and effective solid thermal conductivity on the performance of methane steam reforming carried out in solar volumetric thermochemical reactors are lacking in the literature.

Moreover, in the literature related to numerical investigations of solar thermochemical reactors (and volumetric solar receivers), an upstream (entry) fluid region to the inlet section is rarely applied. This is particularly relevant if combined with inappropriate inlet boundary conditions to the set of governing equations — such as first-type (Dirichlet) boundary conditions for governing equations featuring diffusive terms applied at boundaries with very high gradients. (Note that very steep gas temperature and species mass fraction profiles establish at the reactor inlet section.) Several works clearly state the application of Dirichlet inlet boundary conditions along with transport equations including diffusive terms and neglecting the application of an upstream fluid region — that would be required to minimize gradients at the inlet section —, see Refs. [12,20,47–49]. Issues related to non-conservation of solved scalars may arise applying inappropriate boundary conditions or, similarly, due to an unsuitable computational domain for a specific kind of boundary conditions. In the literature, authors from other fields deal with this issue (solved scalars full-conservation) by applying Danckwerts boundary conditions that allow to consider simultaneously advective and diffusive fluxes without applying an upstream fluid region — to decrease the relevance of diffusive fluxes at the inlet section — and still, considering diffusion transport mechanisms in the governing equations — see Refs. [50–53].

For LTNE models, numerical investigations on solar reforming reactors have generally considered the net thermal energy consumption by surface-catalyzed (heterogeneous) chemical reactions (reaction heat) accounted for in the gas-phase energy balance. However, the reaction heat is assigned to the solid-phase energy balance by other authors working in the field of solar thermochemical reactors — particularly, based on redox cycles [12,13] —, and by the majority of authors in closely-related areas that apply the same kind of porous and supported catalyst reactors (heterogeneous catalytic reactors) for similar applications — although not considering concentrated solar power as the energy source [54–58]. This last assumption relies on the fact that since reactions take place at the surface of the solid phase, the reaction heat should be accounted for in the solid-phase energy balance because the thermal resistance between the solid surface and the bulk solid phase is lower than between the solid surface and the bulk gas phase. Assigning the reacting heat from surface reactions to the solid-phase energy balance has been applied from the first records of numerical modeling works on heterogeneous (catalytic) reactors — see Ref. [59]. The only reaction heat contribution assigned to the gas-phase energy balance that is usually considered in the literature corresponds to the net heat consumption/release due to homogeneous (gas-phase) chemical reactions. To the authors' knowledge, no investigation is available on the impact of assigning the reaction heat from surface (catalytic) reactions to the gas-phase energy balance for solar thermochemical reforming reactors.

The applied mathematical and numerical models have been poorly described in many papers of this field. This may hinder the feasibility of results reproduction and comparison with other works. In some works, governing equations are missing. Frequently, an incomplete set of boundary conditions are provided — only for particular solved scalars and for a limited number of domain boundaries (generally, neglecting the lateral wall) — and zero-radial derivatives at the exit section have also been (misleadingly) stated and repeated in different works. The principle of dimensional homogeneity has been violated in several works while summing different contributions for governing equation source terms having different dimensions. Furthermore, closure models and the required coefficients for computing species diffusive or gas mixture heat conduction transport rates have also not been provided in many works. Some authors neglect species diffusion and gas-phase thermal diffusion transport mechanisms [34,38,40]. In other works, the species mass balance equation is not presented [14,60–62] which restricts any direct conclusion about the consideration of species diffusion transport mechanisms in the mathematical model. Moreover, the relevance of species diffusion and gas-phase heat conduction mechanisms has not been analyzed for solar-aided methane steam reforming in volumetric thermochemical reactors.

In this work, the effect of different modeling assumptions and closure models that have been frequently considered in the literature of solar thermochemical reactors and closely-related application areas is investigated. Different modeling assumptions and closure models may affect the results accuracy and compromise a meaningful comparison across literature works. Particularly, the following is herein investigated: (i) the role of upstream and downstream fluid regions to the two-phase reactor region; (ii) relevance of species and gas-phase thermal diffusion mechanisms; (iii) reaction heat accounted for in gas- or solid-phase energy balance equations; (iv) LTE vs. LTNE models; (v) model dimension (1D vs. 2D axisymmetric models); (vi) local volumetric convection heat transfer correlations; and (vii) effective solid thermal conductivity correlations. (The last two topics of this investigation (topics (vi)–(vii)) are concerned with the application of different closure models while the remaining topics are related to modeling assumptions.) Prior to the investigation on the impact of the stated assumptions and models, chemical equilibrium calculations are presented to provide guidance on the actual reactor performance and a detailed characterization of the reactor operation is analyzed considering two operation modes: non-reactive and reactive. Reactor

geometric parameters, material properties, and operating conditions are defined in full accordance with typical values observed in previous works to enlarge the relevance of this study among the literature available. Although this investigation is carried out considering methane steam reforming in a volumetric reactor, the relevance of this work extends well beyond solar thermochemical applications since similar models and assumptions have also been widely applied for predicting the performance of volumetric solar absorbers.

This paper is organized as follows. In the next section (Section 2), the physical model of the solar reactor herein considered is introduced. In Section 3, the reference mathematical and numerical models are presented in detail and, subsequently, validated against benchmark data gathered from different references. The results are presented and discussed in Section 4. Finally, brief conclusions are provided in Section 5.

2. Physical model — concentrating solar reactor model description

The physical model of the reactor is presented in Fig. 1. The reactor comprises a ceramic foam structure with a cylindrical shape that is held in place by a tubular housing structure. The reactor radius (R_{react}) and length (L_{react}) are equal to 0.02 m and 0.04 m, respectively. The reactor is placed in the solar collector system in such a way that the focal point of the solar concentration (reflection) system — parabolic dish (not shown in Fig. 1) — is located at the point with x and r coordinates both equal to zero (see the coordinate system in Fig. 1). Calculation of the concentrated solar irradiation distribution at the irradiated (front) reactor section — applying, for instance, Monte Carlo ray tracing algorithms — is outside the scope of this work. Instead, a commonly considered concentrated solar irradiation distribution is prescribed at $x = 0$. For improving the accuracy of numerical predictions, the physical domain of the reactor — particularly, the gas-phase region — is extended upstream and downstream the reactor solid phase, along L_{upstr} and L_{downstr} , respectively — see Fig. 1. The reactive feed gas mixture is provided to the reactor at $x = -L_{\text{upstr}}$. L_{upstr} and L_{downstr} are considered equal to 0.01 m.

The solar thermochemical porous reactor is composed by a silicon carbide (SiC) open-cell foam with the geometrical (morphological) parameters listed in Table 1. The values for this set of parameters were gathered from literature [63]. These values are physically fully consistent with each other since they were evaluated experimentally considering an actual (real) foam sample.

3. Mathematical and numerical models

In this work, the reactor gas and solid phases are described by the volume-averaging approach. A 2D axisymmetric model is considered due to the reactor geometrical and operation symmetry along the

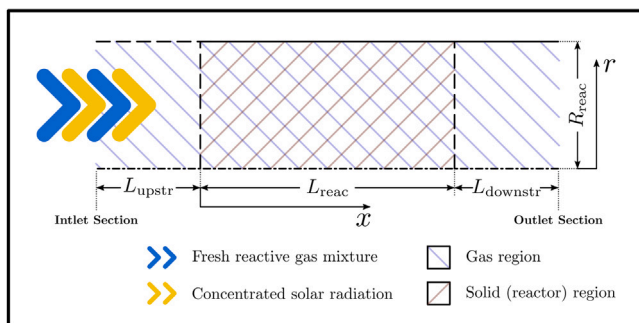


Fig. 1. Schematic (two-dimensional axisymmetric) representation of the solar thermochemical reactor.

Table 1

Geometrical parameters of the SiC foam (reactor porous structure).

Geometrical parameter	Value
Specific surface area, a_v [m^{-1}]	2360
Cell diameter, d_c [m]	1.65×10^{-3}
Pore diameter, d_p [m]	7.17×10^{-4}
Porosity, ϕ [-]	0.87

angular direction. Nevertheless, the governing equations and boundary conditions are presented in a coordinate-free vector form.

The set of equations described in this section comprises the reference mathematical model. The relevance of particular modeling assumptions and closure models is investigated by tailoring the reference mathematical model accordingly and comparing the corresponding results to the results computed with the reference model.

3.1. Governing equations

3.1.1. Continuity and momentum balance equations

The overall mass conservation (continuity) equation and the momentum balance equations along each coordinate direction are given by Eqs. (1) and (2), respectively. In these equations, ρ_g , μ_g , ϕ , \mathbf{u} , and p correspond to the gas density, dynamic viscosity, foam porosity, superficial velocity, and pressure, respectively.

$$\phi \frac{\partial \rho_g}{\partial t} + \nabla \cdot (\rho_g \mathbf{u}) = 0 \quad (1)$$

$$\phi \frac{\partial (\rho_g u_i)}{\partial t} + \nabla \cdot (\rho_g u_i \mathbf{u}) = \nabla \cdot \left\{ \mu_g \nabla u_i + \left[\mu_g (\nabla \mathbf{u})^T - p - \frac{2}{3} \mu_g \nabla \cdot \mathbf{u} \right] \mathbf{i}_i \right\} + S_{M,i} \quad (2)$$

To account for momentum losses in the porous foam (reactor) region, non-negligible momentum source terms are considered. The source term for each component of the momentum balance equations is computed taking into account the viscous and inertial permeability coefficients for the Darcy–Forchheimer pressure drop correlation derived experimentally by Chen et al. [15] — see Eq. (3). These coefficients were developed considering foams with porosity values between 0.87–0.97 and for the range $20 \leq \rho_g |\mathbf{u}| d_p / (\phi \mu_g) \leq 2800$. Other body forces are neglected in momentum source terms.

$$S_{M,i} = -\frac{44.5}{\phi d_p^2} \mu_g u_i - \frac{0.55}{\phi^2 d_p} \rho_g |\mathbf{u}| u_i \quad (3)$$

Eqs. (1) and (2) apply to the entire reactor domain — including upstream and downstream the reactor (single-phase (fluid) regions). However, upstream and downstream the reactor, the porosity is set equal to unity and no momentum source terms are applied. (Although the model is applied for steady-state and incompressible flow conditions, Eqs. (1) and (2) *et seq.* retain the related terms for the sake of completeness and generality as it is usual in the literature.)

3.1.2. Species mass balance equations

The reactor is assumed to operate under the kinetic control. Species mass balance equations are given by Eq. (4), where Y_k corresponds to the species k mass fraction. The species mass balance equations account simultaneously for the advective and diffusive transport mechanisms — second and first terms on the left-hand side (LHS) and right-hand side (RHS), respectively, of Eq. (4). Species diffusive mass fluxes are computed with Eq. (5), according to which species diffusion is driven by species mass fraction (spatial) gradients and also by gas temperature (T_g) gradients (Soret effect). Species (mixture-averaged) diffusion coefficients (D_{km}) and thermal diffusion coefficients (D_k^T) are calculated as stated in the upcoming sections — see Section 3.2. Species mass production/depletion rates due to heterogeneous reactions — chemical reactions taking place on active (catalytic) sites that are available on

the solid structure (foam) surface — are accounted for through the last term on the RHS of Eq. (4).

$$\phi \frac{\partial (\rho_g Y_k)}{\partial t} + \nabla \cdot (\rho_g Y_k \mathbf{u}) = -\nabla \cdot \mathbf{J}_k + \dot{\omega}_k W_k \quad (4)$$

$$\mathbf{J}_k = -\rho_g \phi D_{km} \nabla Y_k - \phi D_k^T \frac{\nabla T_g}{T_g} \quad (5)$$

Species volumetric production rates on a molar basis are computed according to Eq. (6), where \dot{s}_k and the product $a_v F_{\text{cat}/\text{geo}}$ correspond to the species molar production rates per unit active surface area and to the catalytically active specific surface area, respectively. Surface chemical production rates are evaluated at the reactor solid-phase temperature (T_s) — unless otherwise stated. Surface chemistry is only accounted for in the reactor porous region domain — $0 < x < L_{\text{reac}}$ and $0 < r < R_{\text{reac}}$ (see Fig. 1).

$$\dot{\omega}_k = \dot{s}_k (Y_k, T_s) a_v F_{\text{cat}/\text{geo}} \quad (6)$$

The homogeneous (gas-phase) conversion pathway between reactants and products is herein neglected in full accordance with previous works on solar thermochemical applications under reactive [11,19,21] and non-reactive operation modes [30,60]. This is also a common assumption for millisecond contact time catalytic reactors operating at the atmospheric pressure and relying on alternative energy sources to solar radiation to promote endothermic chemical reactions [64–67] but whose relevant fundamental principles and governing equations are basically the same as the ones herein considered.

Upstream and downstream the reactor (two-phase) region, the porosity in Eqs. (4) and (5) is set equal to unity and the species source term does not apply.

3.1.3. Energy balance equations

Unless otherwise stated, the LTNE approach is herein considered to take into account the large temperature differences between solid and gas phases that characterize the operation of thermochemical energy solar applications, particularly near the irradiated (front) section. Therefore, independent energy balance equations for the gas and solid phases are considered.

Gas-phase energy balance equation. Eq. (7) corresponds to the energy balance equation for the reactor bulk gas phase. In Eq. (7), h_g , $\lambda_{g,\text{eff}}$, and h_v are the gas mixture specific enthalpy, effective gas thermal conductivity, and volumetric convection heat transfer coefficient, respectively. The effective gas thermal conductivity is calculated according to Eq. (8), where λ_g is the clear (intrinsic) fluid thermal conductivity — computed as stated in Section 3.2. Eq. (7) accounts for the following energy transport mechanisms: (i) energy advective transport (second term on the LHS); (ii) diffusive transport of energy through heat conduction (first term on the RHS) and due to species mass diffusion (second term on the RHS) — Dufour effect (heat transfer due to species mass fraction gradients) is neglected; and (iii) convective heat transfer (third term on the RHS). Convective heat transfer couples the gas-phase and solid-phase energy balance equations.

$$\phi \frac{\partial (\rho_g h_g)}{\partial t} + \nabla \cdot (\rho_g h_g \mathbf{u}) = \nabla \cdot (\lambda_{g,\text{eff}} \nabla T_g) - \sum_{k=1}^K \nabla \cdot (h_k \mathbf{J}_k) + h_v (T_s - T_g) - S_{\text{chem}} \quad (7)$$

$$\lambda_{g,\text{eff}} = \phi \lambda_g \quad (8)$$

Radiative heat transfer in the gas phase is neglected due to the small optical thickness and to the radiative properties of the gas mixture, in full accordance with the literature. Moreover, under practical conditions of interest (low-speed flow conditions), mechanical compression (Dp/Dt) and viscous dissipation (Φ) effects are negligible, and consequently, the corresponding terms are not featured in the gas-phase energy balance equation.

For the current porous media type (open-cell foam) and fluid flow and thermal conditions, the local volumetric convection heat transfer coefficient can be computed considering the empirical correlation developed with different foam samples applying the transient (single-blow) method by Xia et al. [32] — see Eq. (9), where Re ($\equiv \rho_g |\mathbf{u}| d_p / \mu_g$) and Pr ($\equiv \mu_g c_{p,g} / \lambda_g$) correspond to local Reynolds and Prandtl numbers, respectively. This correlation was developed considering foam samples with porosities in the range 0.87–0.97 and for the range $20 \leq Re \leq 10^3$. This correlation has been applied elsewhere [15,68].

$$h_v = \frac{\lambda_g}{d_p^2} 0.34 \phi^{-2} Re^{0.61} Pr^{1/3} \quad (9)$$

The chemical source term (S_{chem}) is considered in the gas-phase energy balance equation to withdraw any thermal effect (heat consumption) due to chemical reactions from the gas-phase energy balance equation. Note that the adopted formulation for the gas-phase thermal energy balance equation — where the dependent (solved) variable corresponds to the gas mixture specific enthalpy (related to the gas temperature through the corresponding equation of state (Eqs. (26) and (28))) — takes inherently into account the effects of species production/consumption (reaction heat) without applying explicitly the corresponding term as it is required for the energy balance equation formulation considering the temperature as the dependent variable [69–71]. This procedure is applied (unless otherwise stated) because thermal effects of chemical reactions (S_{chem}) are assigned to the solid-phase energy balance equation. Assigning the net thermal effect from catalytic heterogeneous chemical reactions to the solid-phase energy balance equation is a modeling assumption broadly applied in the literature concerning two-phase energy (LTNE) mathematical models developed for predicting the performance of heterogeneous catalyst reactors — see Refs. [55,56,72–75]. However, in the field of concentrated solar power thermochemical applications related to catalytic reforming, thermal effects due to chemical reactions have been assigned to the gas-phase energy balance equation. (Concerning solar $\text{H}_2\text{O}/\text{CO}_2$ -splitting redox cycles and redox hydrocarbon reforming on metal oxide materials, heat consumption at the reduction step and heat release at the oxidation step have been properly considered in the solid-phase energy balance equation — see Refs. [12,13].) The chemical source term is computed considering Eq. (10), where the species specific enthalpy (h_k) is evaluated at the gas (solid) temperature if the species is being consumed (created) according to Eq. (11). This procedure to remove the net heat release/consumption due to surface chemical reactions from the gas-phase energy balance equation — and to assign it to the solid-phase energy balance equation (see Eqs. (12) and (14)) — has been considered elsewhere [76–78].

$$S_{\text{chem}} = - \sum_{k=1}^K h_k(T) \dot{\omega}_k W_k \quad (10)$$

$$h_k(T) = \begin{cases} h_k(T_s), & \dot{\omega}_k \geq 0 \\ h_k(T_g), & \dot{\omega}_k < 0 \end{cases} \quad (11)$$

Outside the two-phase reactor region ($x < 0$ and $x > L_{\text{reac}}$), the convective heat transfer term does not apply, the chemical source term is absent, and the porosity required to compute the effective gas thermal conductivity (Eq. (8)) is set equal to unity.

Solid-phase energy balance equation. The solid-phase energy balance equation is given by Eq. (12). In this equation, $\lambda_{s,\text{eff}}$ corresponds to the effective solid-phase thermal conductivity computed with Eq. (13), where λ_s corresponds to the intrinsic (pure phase) solid thermal conductivity and the one-third factor is included to account for the solid conduction path tortuosity [79,80]. The solid-phase temperature governing equation (Eq. (12)) takes into account heat diffusion in the solid-phase (first term on the RHS), convective heat transfer (second term on the RHS), and a volumetric rate of thermal energy generation (last term on the RHS). The source term of the solid-phase energy balance equation (S_s) is calculated according to Eq. (14) that takes

simultaneously into consideration the net power contribution from radiative heat transfer within the porous structure (S_{rad}) and chemical reactions (S_{chem} — computed in agreement with Eq. (10)). The net radiative heat source term (S_{rad}) takes into account two contributions: (i) the rate of concentrated solar energy locally absorbed; and (ii) the long-wave radiative heat transfer rate within the foam cellular structure including with the surrounding (external and low-temperature) surfaces. This term is computed within the framework of a suitable radiative heat transfer model application.

$$(1 - \phi) \frac{\partial (\rho_s c_{p,s} T_s)}{\partial t} = \nabla \cdot (\lambda_{s,\text{eff}} \nabla T_s) - h_v (T_s - T_g) + S_s \quad (12)$$

$$\lambda_{s,\text{eff}} = \frac{1}{3} (1 - \phi) \lambda_s \quad (13)$$

$$S_s = S_{\text{rad}} + S_{\text{chem}} \quad (14)$$

3.1.4. Radiative transfer equation

Different strategies have been applied in the literature to calculate the net radiative heat transfer for high-temperature volumetric solar applications. Monte Carlo ray tracing has been applied to evaluate the concentrated solar power (short-wave radiative heat contribution) absorbed locally by the solid phase (extinction volume) prior to any computational fluid dynamics (CFD) numerical simulation [9,24,25,47,49]. (In alternative, Beer's law has also been considered [22,26,42,43,81,82], as well as emulating the concentrated solar radiation through a diffusive emission source [8,83–85].) Subsequently, the P1 radiative heat transfer model — that takes into account the long-wave radiative heat transfer — is solved simultaneously with the fluid flow governing equations and solid-phase energy balance equation (with the prescribed short-wave radiative heat transfer contribution computed previously) [9,22,47]. (Alternatively, for the volume-averaging approach, the Rosseland approximation has been applied [20,81,82], and particularly, for discrete pore-scale numerical simulations, the surface-to-surface radiation exchange model (net radiation method) has also been considered [24,86] as well as the discrete ordinates model [26] and discrete transfer radiation model [25] assuming the gas radiatively non-participant.)

In alternative to such a two-step coupling approach, the modified P1 approximation allows the simultaneous consideration of both short-wave (solar) and long-wave (thermal) radiative heat transport. This method has been extensively applied in the literature due to its simplicity and fairly good performance prediction. The modified P1 approximation is given by Eq. (15). In this equation, κ and σ_s are the absorption coefficient and the scattering coefficient, respectively, and G_d and G_c correspond to the diffusive irradiation and collimated (incident) solar irradiation, respectively. The local value of the collimated solar irradiation is calculated with Eq. (16), where q_0'' , β , and x are the concentrated solar irradiation at the reactor irradiated (front) section, the porous foam extinction coefficient, and the local axial position within the reactor, respectively. (The reactor front section is located at $x = 0$ — see Fig. 1.) The radial distribution for the concentrated solar heat flux at the reactor front section — due to the application of concentrator devices, such as a parabolic dish — is commonly considered as an exponential distribution given by Eq. (17) [12]. In this equation, the parameters A and B define the concentrated solar irradiation peak value (observed at $r = 0$ for a non-uniform distribution — distribution for which $B \neq 0$) and the parameter that controls the profile non-uniformity, respectively. (Higher values for B lead to steeper irradiation profiles.)

$$-\nabla \cdot \left(\frac{1}{3(\kappa + \sigma_s)} \nabla G_d \right) = \kappa (4\sigma T_s^4 - G_d) + \sigma_s G_c \quad (15)$$

$$G_c(r, x) = q_0''(r) \exp(-\beta x) \quad (16)$$

$$q_0''(r) = A \exp(-Br^2) \quad (17)$$

After computing the solution for the diffusive irradiation (G_d) — applying Eq. (15) and suitable boundary conditions (see Section 3.3) —, the total irradiation ($G \equiv G_d + G_c$) is calculated and applied to determine the net radiative heat source term for the solid-phase energy balance equation ($S_{\text{rad}} \equiv -\nabla \cdot \mathbf{q}_r = -\kappa (4\sigma T_s^4 - G)$).

3.1.5. Surface chemistry model equations

The species molar production/depletion rates per unit active surface area are evaluated with Eq. (18). In this equation, ν_{ki} , K_g and K_s are the net stoichiometric coefficient for species k in reaction i , the total number of gas-phase species, and the total number of surface (adsorbed) species considered in the detailed surface reaction mechanism, respectively.

$$\dot{s}_k(Y_k, T_s) = \sum_{i=1}^I \nu_{ki} k_i \prod_{j=1}^{K_g+K_s} c_j^{\nu_{ji}} \quad (18)$$

The concentration of species j (c_j in Eq. (18)) is calculated according to Eq. (19), where θ_j , Γ , and σ_j are the (surface) species j site fraction, the surface site density, and the number of surface sites occupied by the surface species j , respectively.

$$c_j = \begin{cases} Y_j \rho_g / W_j, & \text{gas-phase species} \\ \theta_j \Gamma / \sigma_j, & \text{surface species} \end{cases} \quad (19)$$

The (forward) rate constant of reaction i (k_i in Eq. (18)) is given by Eq. (20) for adsorption reactions and by Eq. (21) for surface and desorption reactions. (Eq. (21) presents a modified Arrhenius expression with surface coverage dependency — parameters μ_{ki} and ϵ_{ki} that modify the pre-exponential factor (A_i) and activation energy (E_i), respectively). In Eq. (20), γ_i and τ are the sticking coefficient of gas-phase species i and the sum of the stoichiometric coefficients of all surface reactants, respectively, in the adsorption reaction of species i . The solid-phase reactor temperature is considered to compute the reaction rate constants.

$$k_i = \frac{\gamma_i}{\Gamma^\tau} \sqrt{\frac{RT_s}{2\pi W_i}} \quad (20)$$

$$k_i = A_i T_s^{\beta_i} \exp\left(\frac{-E_i}{RT_s}\right) \prod_{k=1}^{K_s} \theta_k^{\mu_{ki}} \exp\left(\frac{-\epsilon_{ki} \theta_k}{RT_s}\right) \quad (21)$$

Surface species site fractions are governed by Eq. (22). At steady-state conditions, this equation implies a zero net production rate of surface species k . More details on modeling the rates of heterogeneous catalytic reactions can be found elsewhere [87,88].

$$\frac{d\theta_k}{dt} = \frac{\dot{s}_k \sigma_k}{\Gamma} \quad (22)$$

The detailed multistep surface reaction mechanism developed by Deutschmann and co-workers [89] for methane steam reforming over Rh/Al₂O₃ catalysts is herein applied. This mechanism is composed by 48 elementary and irreversible reactions, 6 gas-phase species (CH₄, O₂, H₂O, CO₂, H₂, and CO), and 12 surface species. The surface site density was set equal to 2.72×10^{-9} mol cm⁻² in full agreement with the literature [64,89].

3.2. Thermophysical and radiative properties

The gas mixture density is computed applying the ideal gas law — Eq. (23), where \bar{W} corresponds to the gas molar weight given by Eq. (24).

$$\rho_g = \frac{\rho \bar{W}}{RT_g} \quad (23)$$

$$\frac{1}{\bar{W}} = \sum_{k=1}^{K_g} \frac{Y_k}{W_k} \quad (24)$$

The gas mixture specific heat and specific enthalpy are calculated with Eqs. (25) and (26), respectively. In these equations, the single

species specific heat and enthalpy are computed according to the temperature polynomials presented by Eqs. (27) and (28), respectively. The species coefficients required in Eqs. (27) and (28) were collected from the GRI-Mech 3.0 database [90].

$$c_{p,g} = \sum_{k=1}^K Y_k c_{p,k} \quad (25)$$

$$h_g = \sum_{k=1}^K Y_k h_k \quad (26)$$

$$\frac{c_{p,k} W_k}{R} = a_{1,k} + a_{2,k} T_g + a_{3,k} T_g^2 + a_{4,k} T_g^3 + a_{5,k} T_g^4 \quad (27)$$

$$\frac{h_k W_k}{R} = a_{1,k} T_g + \frac{a_{2,k}}{2} T_g^2 + \frac{a_{3,k}}{3} T_g^3 + \frac{a_{4,k}}{4} T_g^4 + \frac{a_{5,k}}{5} T_g^5 + a_{6,k} \quad (28)$$

The gas mixture dynamic viscosity is computed according to the Wilke formula that is given by Eq. (29), where X_k corresponds to the species mole fraction (calculated considering Eq. (30)) and Φ_{kj} is calculated with Eq. (31).

$$\mu_g = \sum_{k=1}^{K_g} \frac{X_k \mu_k}{\sum_{j=1}^{K_g} X_j \Phi_{kj}} \quad (29)$$

$$X_k = \frac{\bar{W}}{W_k} Y_k \quad (30)$$

$$\Phi_{kj} = \frac{1}{\sqrt{8}} \left(1 + \frac{W_k}{W_j} \right)^{-1/2} \left[1 + \left(\frac{\mu_k}{\mu_j} \right)^{1/2} \left(\frac{W_j}{W_k} \right)^{1/4} \right]^2 \quad (31)$$

The species diffusion coefficients in the gas mixture and the gas mixture thermal conductivity are calculated according to Eqs. (32) and (33), respectively.

$$\frac{1}{D_{km}} = \sum_{j \neq k}^K \frac{X_j}{D_{kj}} + \frac{X_k}{1 - Y_k} \sum_{j \neq k}^K \frac{Y_j}{D_{kj}} \quad (32)$$

$$\lambda_g = \frac{1}{2} \left(\sum_{k=1}^K X_k \lambda_k + \frac{1}{\sum_{k=1}^K X_k / \lambda_k} \right) \quad (33)$$

Pure (individual) species transport coefficients (μ_k , D_{kj} , and λ_k) were computed in accordance with the standard kinetic theory considering the transport database gathered from GRI-Mech 3.0 [90].

For the solid matrix (SiC foam), an intrinsic thermal conductivity (λ_s) equal to 80 W m⁻¹ K⁻¹ is considered in agreement with the literature [12,91]. The radiative properties κ , σ_s , and β are calculated according to Eqs. (34), (35), and (36), respectively, that take into account the foam porosity, strut surface emissivity (ϵ), and foam mean pore diameter (d_p) [92,93]. In this work, the foam strut surface emissivity is set equal to 0.92 in agreement with the literature [9,12,18].

$$\kappa = \frac{3\epsilon(1-\phi)}{2d_p} \quad (34)$$

$$\sigma_s = \frac{3(2-\epsilon)(1-\phi)}{2d_p} \quad (35)$$

$$\beta \equiv \kappa + \sigma_s = \frac{3(1-\phi)}{d_p} \quad (36)$$

3.3. Boundary conditions

At the domain inlet section (Section $x = -L_{\text{upstr}}$ — see Fig. 1), the gas axial and radial (superficial) velocity components are prescribed according to Eqs. (37) and (38), respectively, and the gas temperature and species composition are imposed as stated by Eqs. (39) and (40), respectively. Therefore, Dirichlet (first-type) boundary conditions are considered for the velocity, species mass fractions, and gas mixture temperature (gas mixture specific enthalpy) at the inlet section.

$$u = u_{\text{in}} \quad (37)$$

$$v = 0 \quad (38)$$

$$T_g = T_{g,\text{in}} \quad (39)$$

$$Y_k = Y_{k,\text{in}} \quad (40)$$

At the centerline, axial symmetry conditions are considered for the velocity components (Eqs. (41) and (38)), species mass fractions (Eq. (42)), gas and solid temperatures (Eqs. (43) and (44), respectively), and diffusive irradiation (Eq. (45)). In the equations considered in this section, \mathbf{n} corresponds to the unit outward normal vector to the surface where each equation applies.

$$\nabla u \cdot \mathbf{n} = 0 \quad (41)$$

$$\nabla Y_k \cdot \mathbf{n} = 0 \quad (42)$$

$$\nabla T_g \cdot \mathbf{n} = 0 \quad (43)$$

$$\nabla T_s \cdot \mathbf{n} = 0 \quad (44)$$

$$\nabla G_d \cdot \mathbf{n} = 0 \quad (45)$$

At the outer surface ($r = R_{\text{reac}}$) and for $0 \leq x \leq L_{\text{reac}}$, the no-slip boundary condition (Eq. (46)) is applied, thermal equilibrium between both phases (Eq. (47)) is considered as well as heat flux continuity (Eq. (48)) and the Marshak's boundary condition (Eq. (49)).

$$u = v = 0 \quad (46)$$

$$T_g = T_s \quad (47)$$

$$\lambda_{s,\text{eff}} \nabla T_s \cdot \mathbf{n} = -\lambda_{g,\text{eff}} \nabla T_g \cdot \mathbf{n} + \mathbf{q}_r \cdot \mathbf{n} + U (T_\infty - T_s) \quad (48)$$

$$\mathbf{q}_r \cdot \mathbf{n} \equiv -\frac{1}{3\beta} \nabla G_d \cdot \mathbf{n} = -\frac{\epsilon_w (4\sigma T_w^4 - G_d) + 4(1-\epsilon_w) H_c}{2(2-\epsilon_w)} \quad (49)$$

In Eq. (48), U denotes the overall heat transfer coefficient, which for a perfectly insulated reactor lateral wall is equal to zero. Eq. (48) corresponds to an energy balance applied to the outer reactor surface stating that the sum between the conduction heat flux of the solid phase (first term on the LHS), the conduction heat flux of the gas phase (first term on the RHS), and the heat flux lost through the outer reactor surface to the external environment (third term on the RHS) must equal the net radiative heat flux to the lateral wall (second term on the RHS — calculated in accordance with Eq. (49)). In the literature, the radiative heat flux contribution in Eq. (48) has been neglected — e.g. Ref. [49]. (In other works, due to the absence of the corresponding boundary conditions it is not even possible to ascertain.) However, considering such an assumption, the net radiative heat flux transferred from the reactor interior volume to the reactor lateral wall (calculated with the application of the Marshak's boundary condition to the modified P1 approximation) is lost from the computational domain without any physical reason. This assumption may constitute a violation to the reactor overall energy conservation. The radiative heat flux term is exactly negligible if the surface reflectivity were equal to unity (emissivity equal to zero once the lateral surface is opaque). The same correlation for the effective solid thermal conductivity (Eq. (13)) is herein applied in Eqs. (12) and (48) because the Fourier's law (considered to develop these equations from the first law of thermodynamics) is the same ($q_s'' = -\lambda_{s,\text{eff}} \nabla T_s$). (Some authors have considered different (inconsistent) expressions for the effective solid thermal conductivity in the interior region and at the domain boundary, that is in Eqs. (12) and (48), respectively — see e.g. Refs. [49,94].)

At the outer surface ($r = R_{\text{reac}}$) and for $x > L_{\text{reac}}$, Eqs. (46), (42), and (43) are considered while for $x < 0$, Eqs. (38), (41), (42), and (43) apply. At $x = 0$ and $x = L_{\text{reac}}$, Eqs. (44) and (49) are considered for the solid-phase energy balance equation and for the modified P1 model equation, respectively. (Note that since heat transfer by radiation and convection is considered as a volumetric phenomenon in the current model formulation, radiative and convective heat losses from the solid phase at the reactor entrance section ($x = 0$) are properly taken into account in the governing equations instead of being directly considered at the boundaries. Therefore, a duplicate consideration of radiative heat losses from the reactor entrance section is avoided.) In Eq. (49), T_w , ϵ_w , and H_c corresponds to the wall temperature, wall emissivity, and wall collimated irradiation, respectively. At the lateral wall, the wall temperature corresponds to the local solid temperature (equal to the local gas temperature), while at Sections $x = 0$ and $x = L_{\text{reac}}$ the wall temperature is set equal to the inlet gas temperature ($T_{g,\text{in}}$) and to the average reactor outlet gas temperature ($\bar{T}_{g,\text{out}}$), respectively. In accordance with previous works, the wall emissivity is set equal to unity for all sections where Marshak's boundary conditions apply [45,94,95]. H_c is negligible at the lateral wall since the concentrated solar flux is parallel to the reactor centerline.

At the outlet section, negligible gradients along the axial direction for the solved variables are considered as well as a negligible static pressure.

3.4. Numerical models

The mathematical model is numerically solved through the application of STAR-CCM+ software — a finite-volume based CFD code supported and made commercially available by Siemens. Geometry design and mesh generation were carried out within the STAR-CCM+ framework. The convective terms of the momentum, gas-phase energy, and species mass balance equations are discretized considering the second-order upwind differencing scheme. The pressure–velocity coupling as well as the solution of the whole system of linear algebraic equations — derived from the discretization of governing equations and boundary conditions — are based on SIMPLE algorithm. The stopping criterion that establishes a converged solution is dictated by a maximum residual below 10^{-6} for all solved balance equations.

Since the radiative heat transfer model herein considered (P1 approximation) is not natively available (embedded) in STAR-CCM+, the STAR-CCM+ passive scalar feature was considered to implement this model — note that the P1 model governing equation corresponds to a steady diffusion equation with a source term (non-homogeneous Helmholtz equation). Moreover, overlapping solution domains were considered for computing solid and gas temperatures and diffusive irradiation (solved variable of the P1 model), each one discretized taking into account the same mesh features. This strategy allowed to couple the solution for such solved variables minimizing interpolation errors. Iteratively updating tables storing the solution for the relevant variables were applied to transport and make available the solution fields across the solution domains (data mapping procedure). Field functions (user defined functions) were developed within STAR-CCM+ framework to compute local source terms for governing equations, volumetric convection heat transfer coefficients, and boundary conditions.

Pure species viscosities, thermal conductivities, binary diffusion coefficients, and thermal diffusion coefficients were evaluated with the open-source code package CANTERA [96] as well as mixture dynamic viscosities, mixture thermal conductivities, and species diffusion coefficients (mixture-averaged diffusion coefficients). The heterogeneous rates of species production/depletion were computed with the kinetic interpreter available in CANTERA. CANTERA was coupled with STAR-CCM+ through the development of externally coded user functions (user code). CANTERA was also applied independently for chemical equilibrium calculations.

3.5. Model validation

The suitable implementation and prediction capability of the models presented before are herein assessed by comparing the corresponding numerical model results to appropriate benchmark data available in the literature. Three model validation cases are considered, each one assigned to the following: (i) radiative heat transfer model (P1 approximation); (ii) hydrothermal model (fluid flow governing equations, LTNE energy balance equations, and modified P1 approximation); and (iii) chemical kinetics and species transport models. Each validation case is addressed in the following sections — see Sections 3.5.1 to 3.5.3.

3.5.1. Radiative heat transfer model

The P1 approximation is applied to evaluate the non-dimensional temperature distribution governed by conduction and radiative heat transfer in a 1D planar absorbing and emitting medium. The walls (medium boundaries) — that are assumed as black and diffusive surfaces — are kept at different temperatures ($T(x=0) = T_{s,1}$ and $T(x=L) = T_{s,2}$) being the ratio between these temperature values ($T_{s,1}/T_{s,2}$) equal to 0.5. The model was applied considering an optical thickness ($\tau \equiv \beta L$) equal to 1.0 and three different conduction–radiation parameter ($N \equiv \lambda\beta / (4\sigma T_{s,1}^3)$) values: 0.01; 0.1; and 1.0. Benchmark data gathered from Talukdar and Mishra [97] and Chen et al. [91] are considered as reference results for the problem and boundary conditions under consideration. Fig. 2 presents the comparison between the current results and the reference results from where a fairly good agreement is concluded.

3.5.2. Hydrothermal model

The hydrothermal model is applied to a specific problem and conditions considered by Chen et al. [91] to assess the current model prediction capability (model verification). In accordance with the reference work, a volumetric solar receiver composed by a SiC foam absorber with porosity and mean cell diameter equal to 0.9 and 2.0 mm, respectively, is considered. The absorber has an outer radius and length equal to 0.03 m and 0.05 m, respectively. At the absorber front section, air at a temperature of 300 K and with a velocity (aligned with the receiver centerline) equal to 0.8 m s^{-1} is considered. The concentrated solar irradiation distribution at the front section is given by $q_0'' [\text{W m}^{-2}] = 1.5 \times 10^6 \exp(-2560 r [\text{m}]^2)$. The outer absorber surface ($r = R$) is perfectly insulated. The thermophysical properties provided in the reference work are considered. The modified P1 approximation is considered to account for the concentrated solar radiation absorption and radiative heat transfer. Figs. 3(a) and (b) present the comparison between the results obtained in this work and the reference results for gas and solid temperature profiles (along the receiver centerline) and radial solid temperature profile at the absorber front section,

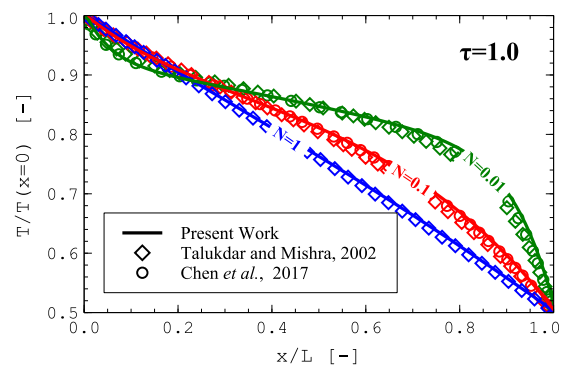


Fig. 2. Verification of the radiative heat transfer model (P1 approximation): non-dimensional temperature distribution in a 1D planar absorbing and emitting medium.

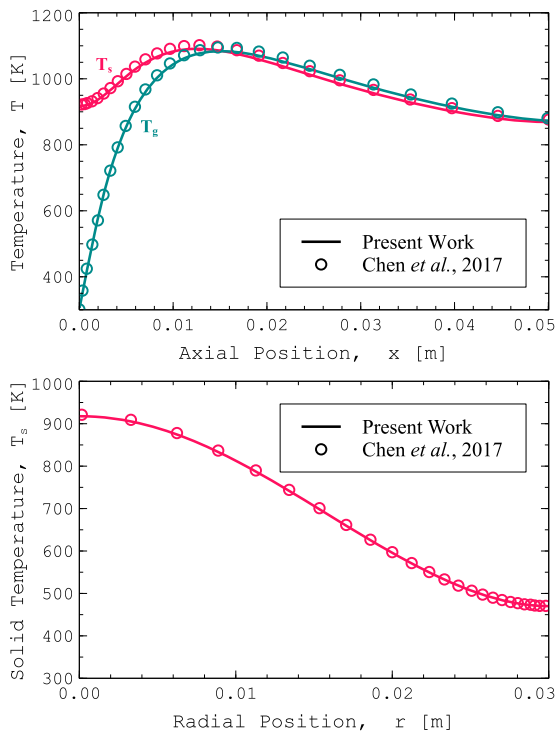


Fig. 3. Verification of the receiver hydrothermal model: (a) solid temperature (T_s) and gas temperature (T_g) profiles at the receiver centerline; and (b) solid temperature profile at the absorber front section. ((a) and (b): top and bottom, respectively. This labeling scheme will apply throughout this document.)

respectively. A good matching is observed between both sets of model results which reinforce the current model verification. Moreover, the reference work reports a pressure drop of 151.3 Pa along the entire absorber and according to the current model implementation a pressure drop value equal to 153.0 Pa (relative error of about 1%) is obtained. All evidence support a successful hydrothermal model verification.

3.5.3. Chemical kinetics and species transport models

The procedure required to evaluate the species production/destruction rates according to a detailed surface reaction mechanism coupled to the species transport solely governed by advection — *i.e.*, a simplified form of Eq. (4) for which the diffusion term is neglected (convection–reaction equation) — is herein assessed. The results of the current model implementation are compared with benchmark data gathered from Dalle Nogare et al. [98] related to catalytic partial oxidation of methane for the production of synthesis gas over Rh supported on Al_2O_3 foam catalysts. The convection–reaction equation is solved in a 1D domain and the surface temperature profile measured experimentally is considered to evaluate the kinetic rates. The detailed reaction mechanism applied in the reference work was similarly considered in this work. In accordance with the values provided in the reference work, the reactor catalytically active specific surface area — the product $a_v F_{\text{cat}/\text{geo}}$ (see Eq. (6)) — was set equal to 8480 m^{-1} . The reactor operates with a feed mixture of CH_4/O_2 composed by 29.1/15.3 on molar basis and Ar to balance. A total volumetric flow rate equal to 5 L min^{-1} evaluated at room temperature and atmospheric pressure is considered. Fig. 4 presents the comparison between the results obtained in this work and the reference results along the reactor axial direction. A general good agreement between both sets of results is observed for all reactive species.

4. Results and discussion

The operating conditions considered to conduct this study are listed in Table 2. Two inlet gas velocities are defined ($u_{\text{in},1}$ and $u_{\text{in},2}$). The

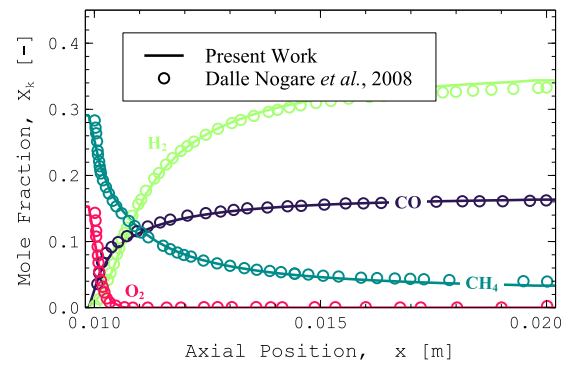


Fig. 4. Verification of chemical kinetics and species transport models: species mole fraction profiles in a methane catalytic partial oxidation reactor.

Table 2

Operating conditions considered in this work.

Parameter	Value
Inlet gas velocity, u_{in} [m s^{-1}]	0.25 ($u_{\text{in},1}$) and 0.50 ($u_{\text{in},2}$)
Inlet gas temperature, $T_{\text{g},\text{in}}$ [K]	300
Inlet gas composition, $X_{k,\text{in}}$ [-]	CH_4 0.25 H_2O 0.75
Concentrated solar heat flux parameters — Eq. (17)	
A [W m^{-2}]	1.5×10^6
B [m^2]	2560

inlet gas velocity values as well as the mixture composition herein considered are commonly within the range of interest observed in the literature — see Refs. [14,18,22,60]. The gas mixture is provided to the reactor at the ambient temperature. The values for parameters A and B (Eq. (17)) are also widely applied in literature to describe the incident solar irradiation profile in a parabolic dish solar collector assembly [12,94,99]. The reactor operates at a reference pressure equal to $1.01325 \times 10^5 \text{ Pa}$ (1 atm). Negligible heat losses through the reactor lateral wall are considered — $U = 0$ (adiabatic surface). $F_{\text{cat}/\text{geo}}$ was set equal to 1.0 in full agreement with the assumption of negligible (internal) diffusion limitations within the catalyst layer since this value is compatible with the absence of a thick washcoat layer applied onto the inert ceramic foam. (Moreover, due to the high working temperatures, a stable long-term reactor operation with a thick and highly porous washcoat layer having a high metal dispersion would be challenging due to thermal-driven catalyst deactivation issues.) A relatively low $F_{\text{cat}/\text{geo}}$ value also minimizes the relevance of external mass transfer resistances.

The remainder of this section is organized as follows. In the following subsection (Section 4.1), chemical equilibrium calculations considering the operating condition (inlet gas mixture composition, temperature, and pressure) under consideration are presented (Section 4.1.1) and the reactor hydrodynamic, thermal, and chemical performance is thoroughly analyzed (Section 4.1.2). The impact of different modeling assumptions and closure models is presented in Section 4.2. Particularly, the relevance of expanding the computational domain upstream and downstream the reactor inlet and outlet sections, respectively, is investigated in Section 4.2.1. The importance of species and gas-phase thermal diffusion transport mechanisms is evaluated in Section 4.2.2. In Section 4.2.3, two distinct procedures to account for the reaction heat in LTNE energy balance equations are discussed. The effect of considering a LTE model is investigated in Section 4.2.4. 1D model results are compared with 2D axisymmetric model predictions in Section 4.2.5. Finally, the comparison between the reactor performance predicted with two different correlations (closure models) for the volumetric

convection heat transfer coefficient and for the effective solid thermal conductivity is analyzed in Sections 4.2.6 and 4.2.7, respectively.

4.1. Reactor full performance characterization

4.1.1. Chemical equilibrium state analysis

Fig. 5 presents chemical equilibrium calculations for several reactor integral performance parameters: (i) reactants conversions (χ_{CH_4} and $\chi_{\text{H}_2\text{O}}$); (ii) syngas selectivities (S_{H_2} and S_{CO}); (iii) ratio between chemical (energy storage) efficiency and thermochemical efficiency ($\eta_{\text{chem}}/\eta_{\text{th}}$); and (iv) gas temperature. Eqs. (50) to (53) present the definition for reactant species k conversion, H_2 and CO selectivities, and for the ratio between chemical efficiency and thermochemical efficiency at equilibrium conditions. Equilibrium values are eventually observed if the mixture residence time in the reactor is sufficiently high — for long reactors or at low inlet gas velocity values.

$$\chi_k^{\text{equil}} = \frac{Y_{k,\text{in}} - Y_k^{\text{equil}}}{Y_{k,\text{in}}} \quad (50)$$

$$S_{\text{H}_2}^{\text{equil}} = \frac{X_{\text{H}_2}^{\text{equil}}}{X_{\text{H}_2}^{\text{equil}} + X_{\text{H}_2\text{O}}^{\text{equil}}} \quad (51)$$

$$S_{\text{CO}}^{\text{equil}} = \frac{X_{\text{CO}}^{\text{equil}}}{X_{\text{CO}}^{\text{equil}} + X_{\text{CO}_2}^{\text{equil}}} \quad (52)$$

$$\frac{\eta_{\text{chem}}^{\text{equil}}}{\eta_{\text{th}}} = \frac{h_g(Y_k^{\text{equil}}, T_{g,\text{in}}) - h_g(Y_{k,\text{in}}, T_{g,\text{in}})}{Q_0 \eta_{\text{th}} / \dot{m}} \quad (53)$$

For chemical equilibrium calculations, the same gas-phase species taken into account in the detailed surface reaction mechanism (see Section 3.1.5) are considered. The equilibrium values for the parameters under consideration were computed considering the inlet mixture temperature and composition defined in Table 2 along a specific absorbed energy ($Q_0 \eta_{\text{th}} / \dot{m}$) range from 0 to about 7 MJ kg^{-1} . (The specific absorbed energy corresponds to the total power absorbed by the reactive gas mixture at the reactor outlet section — from where heat losses are assumed as negligible — per unit mass flow rate.) The specific enthalpy and pressure (1 atm) were held constant between the initial and equilibrium states. The specific enthalpy is calculated as a function of the specific absorbed energy and inlet mixture composition and temperature according to Eq. (54).

$$h_g^{\text{equil}} = h_g(Y_{k,\text{in}}, T_{g,\text{in}}) + Q_0 \eta_{\text{th}} / \dot{m} \quad (54)$$

Chemical equilibrium calculations reveal that methane conversion increases almost linearly with the specific absorbed energy attaining 99% at $Q_0 \eta_{\text{th}} / \dot{m}$ approximately equal to 4.7 MJ kg^{-1} — see Fig. 5. Equilibrium CO selectivity also increases monotonically upon increasing the specific absorbed energy, even though equilibrium mixture conditions with a negligible amount of CO_2 (i.e., $S_{\text{CO}}^{\text{equil}}$ equal to one) are not observed in the $Q_0 \eta_{\text{th}} / \dot{m}$ range considered. Equilibrium H_2O conversion, H_2 selectivity, and $\eta_{\text{chem}}/\eta_{\text{th}}$ ratio present maximum values — approximately equal to 46.5%, 67.6%, and 58.3%, respectively — in the $Q_0 \eta_{\text{th}} / \dot{m}$ range 4.3–4.6 MJ kg^{-1} , for which the equilibrium gas temperature is located in the range 954–995 K. A set of operating conditions (Q_0 and \dot{m}) combined with a reactor operation (η_{th}) that together promote specific absorbed energy values in the stated range is highly recommended to achieving high fuel conversion and syngas selectivities, and a high chemical efficiency value in relation to thermal efficiency — that is, the energy is preferentially converted into chemical energy instead of thermal (sensible internal) energy. Considering the current reactor radius (R_{react}) and the values listed in Table 2, Q_0 / \dot{m} is approximately equal to 5.27 MJ kg^{-1} ($u_{\text{in},1}$). Consequently, a reactor design for which the thermochemical efficiency lies in between 81.6% and 87.3% ($u_{\text{in},1}$) would be required to obtain a high value of methane conversion and the maximum values for H_2O conversion, H_2 selectivity, and $\eta_{\text{chem}}/\eta_{\text{th}}$ ratio at equilibrium conditions. For the highest

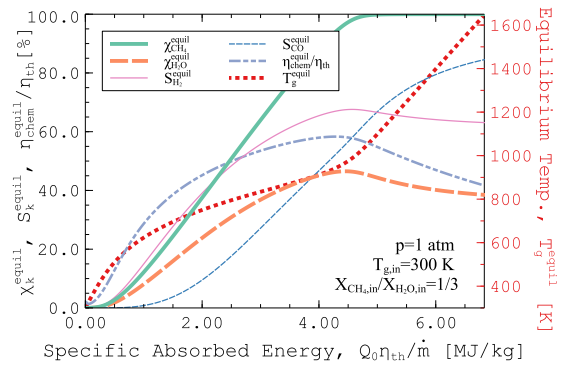


Fig. 5. Chemical equilibrium predictions for CH_4 and H_2O conversion ($\chi_{\text{CH}_4}^{\text{equil}}$ and $\chi_{\text{H}_2\text{O}}^{\text{equil}}$), H_2 and CO selectivity ($S_{\text{H}_2}^{\text{equil}}$ and $S_{\text{CO}}^{\text{equil}}$), ratio between chemical efficiency and thermochemical efficiency ($\eta_{\text{chem}}^{\text{equil}}/\eta_{\text{th}}$) and temperature (T_g^{equil}) as a function of the specific absorbed energy. As initial state conditions, a CH_4 – H_2O gas mixture with a molar ratio ($\text{CH}_4/\text{H}_2\text{O}$) equal to 1/3 and a temperature equal to 300 K is considered.

inlet gas velocity considered ($u_{\text{in},2}$), the specific absorbed energy range 4.3–4.6 MJ kg^{-1} cannot even be achieved since the reactor would have to be operating with a higher than possible thermochemical efficiency (i.e., $\eta_{\text{th}} > 1$).

4.1.2. Reactor hydrodynamic, thermal, and chemical performance analysis

The reactor performance is herein analyzed in detail for two distinct reactor operation modes: non-reactive (inert) and reactive. The non-reactive operation mode would be observed for a reactor with a negligible catalytic activity (inert porous structure). Additionally, the two operating conditions listed in Table 2 — differing only on the inlet gas velocity (u_{in}) — are considered in this study.

Fig. 6 presents temperature distributions for the reactor solid and gas phases considering the non-reactive and reactive operation modes at the lowest inlet gas velocity value ($u_{\text{in},1}$). Figs. 7(a) and (b) present solid- and gas-phase temperature profiles along the reactor axial direction for the two inlet gas velocity values, considering the non-reactive and reactive modes of operation, respectively. In these figures, for each phase and operating condition (inlet gas velocity), three profiles are presented: (i) the reactor centerline ($r = 0$) profile; (ii) the reactor lateral wall ($r = R_{\text{react}}$) profile; and (iii) the radial average profile. For each axial location, radial-averaged gas temperatures (T_g^{avg}) are computed in full compliance with radial-averaged values for the mixture specific enthalpy and species mass fractions — see Eq. (55).

$$T_g^{\text{avg}} = T_g(h_g^{\text{avg}}, Y_k^{\text{avg}}) \quad (55)$$

Since the axial component of the mass flux (ρu) is not uniform along the radial coordinate, the radial-averaged mixture specific enthalpy and species mass fractions are calculated with Eqs. (56) and (57), respectively.

$$h_g^{\text{avg}} = \frac{\int_A \rho u \sum_{k=1}^K Y_k h_k dA}{\dot{m}} \quad (56)$$

$$Y_k^{\text{avg}} = \frac{\int_A \rho u Y_k dA}{\dot{m}} \quad (57)$$

Table 3 presents several reactor performance parameters for the non-reactive and reactive operation modes considering the two operating conditions. The thermochemical efficiency is calculated with Eq. (58), where the numerator corresponds to the net thermal power transferred from the solid phase to the fluid — and converted to chemical and sensible thermal energy (thermochemical energy) — from the reactor inlet section to the outlet section. The denominator (Q_0) corresponds to the total concentrated solar power provided to the reactor — computed according to Eq. (59), which for the conditions under consideration gives a value approximately equal to 1179.65 W. (For the non-reactive

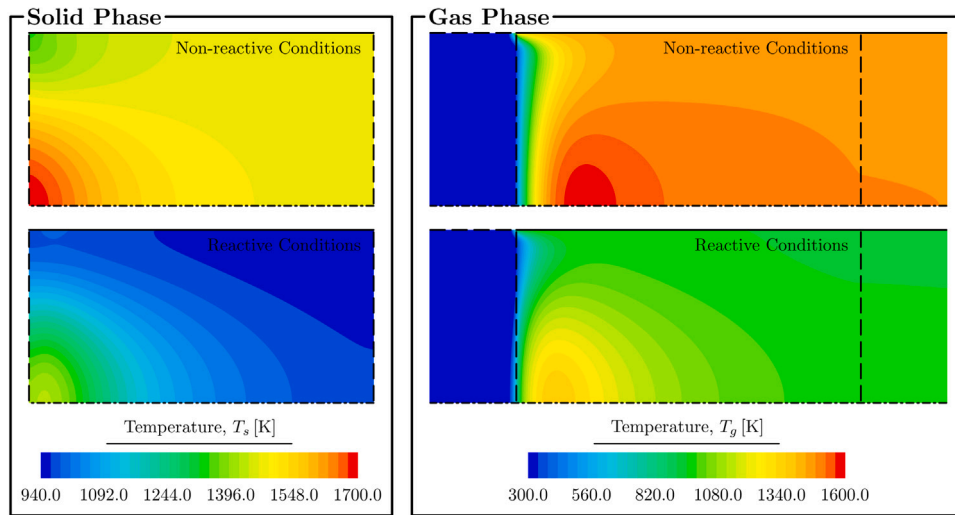


Fig. 6. Temperature distribution for the solid phase (left) and gas phase (right) considering the non-reactive operation (top) and the reactive operation (bottom) for the inlet gas velocity $u_{in,1}$.

Table 3
Performance parameters for the non-reactive and reactive operation modes considering two operating conditions — see Table 2.

Parameter	Operating condition			
	Non-reactive mode		Reactive mode	
	$u_{in,1}$	$u_{in,2}$	$u_{in,1}$	$u_{in,2}$
η_{th} [%]	59.3	74.7	77.3	81.3
η_{chem} [%]	—	—	43.5	29.7
X_{CH_4} [%]	—	—	84.7	30.6
X_{H_2O} [%]	—	—	39.5	17.0
S_{H_2} [%]	—	—	61.3	31.1
S_{CO} [%]	—	—	60.2	33.2
H_2/CO [-]	—	—	5.6	11.0
$T_{s,max}$ [K]	1696.0	1483.1	1420.0	1174.6
T_s^{avg} [K]	1476.0	1116.4	1004.6	886.6
$T_{g,out}^{avg}$ [K]	1476.2	1105.4	951.7	856.5
Δp [Pa]	229.1	279.6	163.2	216.6

operation mode, the thermochemical efficiency is commonly referred to as thermal efficiency.)

$$\eta_{th} = \frac{\dot{m} (h_{g,out}^{avg} - h_{g,in}^{avg})}{Q_0} \quad (58)$$

$$Q_0 = \int_{A_{front}} q''_0 dA \quad (59)$$

Chemical efficiency, reactants conversions, and H_2 and CO selectivities are computed with Eqs. (50)–(53), where instead of equilibrium values (Y_k^{equil} and X_k^{equil}) average values at the reactor outlet section (i.e., at $x = L_{react} + L_{downstr}$ — see Fig. 1) are considered — i.e., $Y_{k,out}^{avg}$ and $X_{k,out}^{avg}$. ($Y_{k,out}^{avg}$ and $X_{k,out}^{avg}$ are evaluated with Eqs. (57) and (60), respectively, applied at the reactor outlet section.)

$$X_k^{avg} = \frac{\dot{m} Y_k^{avg}}{\int_A \rho u (W_k / \bar{W}) dA} \quad (60)$$

In Table 3, the H_2/CO molar ratio at the reactor outlet section is also presented as well as the maximum and average solid-phase temperatures ($T_{s,max}$ and T_s^{avg}), the outlet average gas-phase temperature ($T_{g,out}^{avg}$), and the pressure drop through the porous reactor region (Δp).

Figs. 6 and 7(a)–(b) show that higher solid and gas temperatures are observed near the reactor centerline, mainly due to the characteristics of the concentrated solar heat flux distribution prescribed at the reactor aperture section — profile given by Eq. (17) with a non-zero parameter

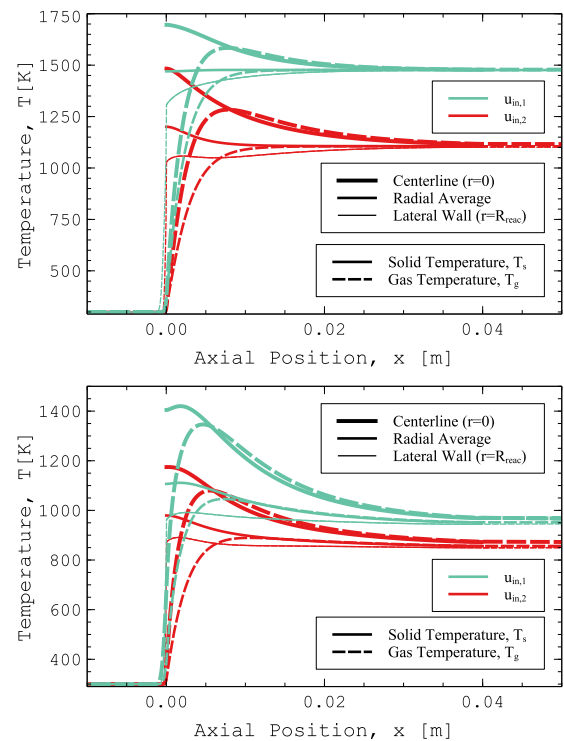


Fig. 7. Axial solid and gas temperature profiles for two inlet gas velocities ($u_{in,1}$ and $u_{in,2}$) and for two different reactor operation modes: (a) non-reactive operation mode; and (b) reactive operation mode.

B (see Table 2). Significant differences are observed in Figs. 7(a)–(b) between the three profiles presented for each operation mode and each inlet gas velocity. For the non-reactive operation mode (Fig. 7(a)), such differences are more remarkable as the inlet gas velocity increases — for the lowest inlet gas velocity, radial and phase thermal equilibrium conditions are observed roughly at the middle of the reactor. For the reactive operation mode (Fig. 7(b)), relevant temperature differences are observed along the entire reactor length across the radial coordinate and between phases, even for the lowest inlet gas velocity. Radial average solid temperature profiles are located in between the corresponding axial solid centerline and reactor outer surface temperature profiles.

Table 4

Net radiative power losses from different reactor sections/surfaces.

Sect./Surf.	Net radiative power loss, $P_{\text{rad, loss}}$ [W]			
	Non-reactive mode		Reactive mode	
	$u_{\text{in},1}$	$u_{\text{in},2}$	$u_{\text{in},1}$	$u_{\text{in},2}$
$x = 0$	479.1	297.6	267.1	220.4
$x = L_{\text{react}}$	0.3	0.7	0.9	0.6
$r = R_{\text{react}}$	14.0	25.3	26.8	27.1

At the reactor lateral wall, the solid and gas phases are in thermal equilibrium (as required by Eq. (47)) — see Figs. 7(a)–(b). Additionally, at the reactor lateral wall, non-adiabatic conditions for the gas and solid phases can also be concluded by the shape of the isotherms (see Fig. 6) which reflect the application of Eqs. (47) and (48).

For the non-reactive operation mode at the lowest inlet gas velocity, Fig. 7(a) shows a modest volumetric effect considering the radial average solid temperature profile — notice that the average solid temperature at the reactor exit section is slightly higher than the average solid temperature at the reactor front section. At the highest inlet gas velocity, the volumetric effect based on the average solid temperature profile becomes absent.

Since an overall endothermic reaction is taking place for the reactive operation mode, lower temperatures are observed for this case under the same set of operating parameters — see Figs. 6 and 7(a)–(b) and Table 3. Due to the lower (solid) temperatures that are registered for the reactive operation mode, lower long-wave radiative heat losses are observed, particularly through the reactor inlet section, and consequently, a higher thermochemical efficiency value is obtained in comparison with the non-reactive operation mode — for the lowest inlet gas velocity, thermochemical efficiency values approximately equal to 77.3% and 59.3% are obtained under the reactive and non-reactive, respectively, modes of operation (see Table 3). (If air (non-reactive O_2/N_2 gas mixture) were considered under the same operating conditions, a thermochemical efficiency equal to about 44.9% would be observed, since higher temperatures would be obtained, and consequently, higher radiation losses — not shown.)

Increasing the inlet gas velocity, lower temperatures and higher thermochemical efficiency values are registered independently of the reactor operation mode — see Figs. 7(a)–(b) and Table 3. Higher thermochemical efficiency values are the outcome of lower radiative heat losses since increasing the gas velocity, convection heat transfer rates increase as well and thermal power is more effectively transferred from the solid phase to the gas phase, avoiding very high solid temperatures, and inevitably, high radiative heat losses. (Note that convection and radiation heat transfer mechanisms are competing against each other for the total absorbed solar energy by the solid phase.)

At the reactor front section ($x = 0$), gas temperatures significantly higher than the inlet temperature ($T_{g,\text{in}}$) are observed due to axial thermal diffusion — see Figs. 6 and 7(a)–(b). This evidence is particularly remarkable near the reactor centerline owing to the high importance of diffusion in relation to advection transport rates. At the reactor centerline (and front section), for the reactive operation mode and the lowest inlet gas velocity, the gas temperature is about 366 K above the inlet gas temperature. (This temperature difference ($T_g(x = 0, r = 0) - T_{g,\text{in}}$) decreases to about 59 K for the highest inlet gas velocity.)

Table 4 presents the total radiative power losses from the reactor interior porous structure through the inlet and outlet sections and to the reactor lateral wall for the two reactor operation modes and the two operating conditions. Fig. 8 presents net radiative heat flux profiles for the reactive operation mode with the two operating conditions at different reactor sections/surfaces. Table 4 shows that the most relevant radiative power loss contribution is observed through the front reactor ($x = 0$) section, independently of the reactor mode of operation and inlet gas velocity. Fig. 8 shows that higher heat flux losses from the reactor front section are registered near the centerline — where higher

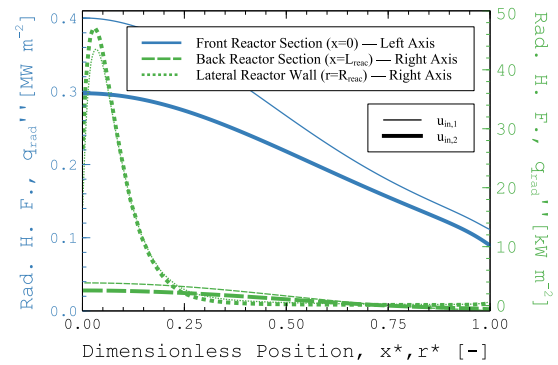


Fig. 8. Net radiative heat flux profiles for the reactive operation mode at three reactor sections/surfaces: front (irradiated) section ($x = 0$); back section ($x = L_{\text{react}}$); and lateral wall surface ($r = R_{\text{react}}$).

solid temperature are also observed — decreasing as the distance to the reactor lateral wall decreases. For the conditions under consideration, radiative heat losses from the reactor outlet section are negligible. Since the reactor lateral wall is opaque and adiabatic, radiative heat losses to the external surroundings are not actual heat losses from the reactor to the external surroundings. This is because the net radiative power absorbed by the lateral wall is transferred back to the internal reactor solid and gas phases by heat conduction — see Eq. (48). (The net radiative power absorbed by the lateral wall corresponds to about 2%–3% of the total power absorbed by the gas mixture for the four cases under consideration. If the radiative heat flux term were not considered in Eq. (48), about that amount of power would be spuriously removed from the system.) Fig. 8 shows that at the reactor lateral wall, the heat flux absorbed by the solid and fluid phases — due to the net radiative power absorption — achieves a maximum value near the reactor front section owing to the high solid temperature that is observed at such axial location but near the reactor centerline. Total power losses through the reactor front section decrease as the inlet gas velocity increases which is in full agreement to the increase on the thermochemical efficiency with the inlet gas velocity concluded previously. Moreover, the total net radiative power absorbed by the lateral wall is higher for higher inlet gas velocity values. This is observed because an increase in the inlet gas velocity promotes a more expressive decrease of the lateral wall temperature (in relation to the temperature decrease at the reactor centerline), and consequently, heat losses from the lateral wall through the reactor front section are also lower in comparison to the radiative heat gains from the reactor interior region as the inlet gas velocity increases.

In addition to the reactor effective power losses observed in Table 4 (power losses through the reactor inlet and exit sections), there is also a permanent power loss related to concentrated solar power transmission through the reactor axial thickness ($P_{\text{trans,loss}} \equiv Q_0 - \int_{V_{\text{react}}} \beta G_c dV$). For a reactor characterized by a low extinction volume (high porosity, high pore diameter, and low reactor thickness (L_{react})), such class of losses can become important. However, in the present case, this power loss is negligible — less than 0.02% of the total concentrated solar power provided to the reactor (Q_0) is lost through transmission.

Fig. 9 presents species mole fraction distributions obtained for the lowest inlet gas velocity ($u_{\text{in},1}$). Figs. 10(a), (b), and (c) present mole fraction profiles for reactants, H_2 and CO , and CO_2 , respectively, along the reactor axial direction for the two inlet gas velocity values. In Figs. 10(a)–(c), three profiles are presented for each operating condition, similarly to Figs. 7(a)–(b): (i) centerline profile; (ii) lateral wall profile; and (iii) radial average profile. Species radial average mole fraction profiles are computed with Eq. (60).

Figs. 9 and 10(a)–(c) show that along the reactor axial direction, the reactant (product) species mole fractions decrease (increase) more

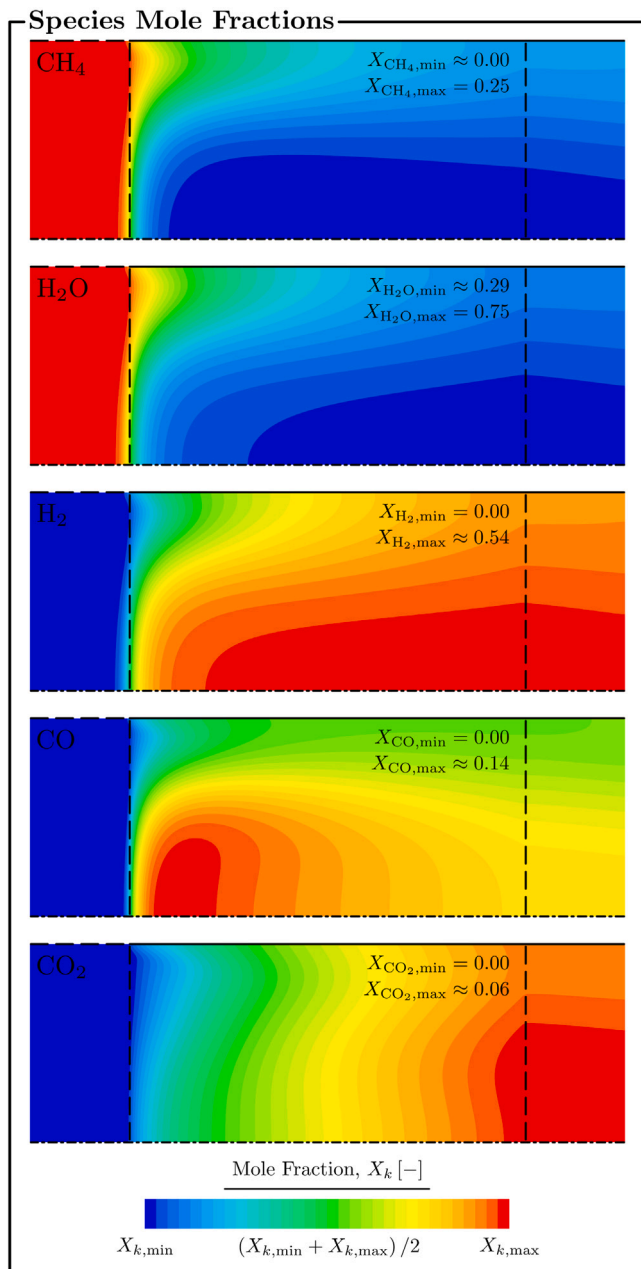


Fig. 9. Species mole fraction distributions for the inlet gas velocity $u_{in,1}$.

rapidly at the centerline than near the reactor outer wall. This evidence is related to the solid temperatures that are higher at the centerline than at the lateral wall — see Fig. 7(b). Consequently, at the reactor outlet section lower (higher) mole fraction values for reactants (products) are observed at the centerline than at the reactor lateral wall. Slightly upstream the reactor front section, products tracing (particularly H₂) and an apparent reactant species consumption (lower reactants mole fractions than the provided values) are observed in Figs. 9 and 10(a)–(c). This is observed due to species diffusion which is particularly relevant at the reactor front section and near the reactor centerline and for low inlet gas velocities. In agreement with Fig. 10(a) and for the highest inlet gas velocity, the mole fractions of reactant species show a slight increase at the centerline downstream of the rapid reactants consumption region — *i.e.* for $x \gtrsim 0.015$ m. This behavior is a sole result of reactant species transport, by both advection and diffusion mechanisms, from the reactor outer regions — wherein due to low

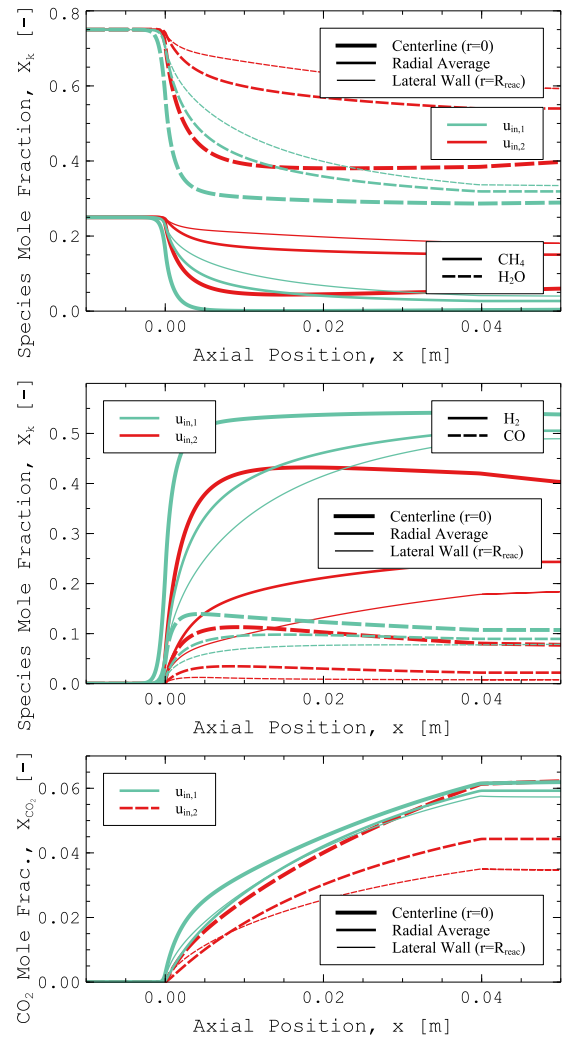


Fig. 10. Axial species mole fraction profiles for two inlet gas velocities ($u_{in,1}$ and $u_{in,2}$): (a) CH₄ and H₂O (reactant species); (b) H₂ and CO; and (c) CO₂. ((a), (b), and (c): top, middle, and bottom, respectively. This labeling scheme will apply throughout this document).

temperatures and low consumption rates, reactants are still abundant — to the centerline. Radial transport (particularly diffusion) is also responsible for the decrease of H₂ mole fraction observed at the reactor centerline for the highest inlet gas velocity — see Fig. 10(b). At the reactor exit section, gas mixture temperature and composition are closer to chemical equilibrium conditions for the lowest inlet gas velocity — for which the residence time is the highest —, as suggested by lower radial differences of gas temperatures and species mole fractions at the reactor exit section — see Figs. 10(a)–(c).

According to Table 3, an increase in the inlet gas velocity leads to a decrease in the chemical efficiency, even though the thermochemical efficiency increases. This evidence means that heat losses decrease upon increasing the inlet gas velocity but the concentrated solar energy absorbed by the solid phase is preferentially transported to the flowing gas mixture than consumed by surface reactions, and consequently, stored as chemical energy. Accordingly, convection heat transfer takes advantage over heat consumption from the solid phase by chemical reactions as the inlet gas velocity increases. Therefore, the increase in the inlet gas velocity leads to a decrease in the reactants conversions as observed in Table 3. Additionally, H₂ and CO selectivity values also decrease but the H₂/CO ratio increases upon increasing the inlet gas velocity (see Table 3).

Table 5

Performance parameters for three different computational domains considering two operating conditions — see Table 2.

Parameter	Computational domain				
	N-UR		N-DR	UDR	
	$u_{in,1}$	$u_{in,2}$	$u_{in,1}$	$u_{in,1}$	$u_{in,2}$
η_{th} [%]	76.4	80.8	77.4	77.3	81.3
Ω_{th} [%]	3.1	0.9	0.0	0.0	0.0
η_{chem} [%]	41.9	28.7	43.7	43.5	29.7
χ_{CH_4} [%]	83.4	29.8	84.8	84.7	30.6
χ_{H_2O} [%]	39.4	16.8	39.5	39.5	17.0
S_{H_2} [%]	59.9	30.4	61.4	61.3	31.1
S_{CO} [%]	57.0	29.4	60.2	60.2	33.2
H_2/CO [-]	5.7	12.3	5.6	5.6	11.0
$T_{s,max}$ [K]	1251.3	1102.5	1420.0	1420.0	1174.6
$T_{g,avg}^{in}$ [K]	984.8	883.3	1004.8	1004.6	886.6
$T_{g,avg}^{out}$ [K]	940.9	855.7	952.8	951.7	856.5
Δp [Pa]	154.7	214.1	163.6	163.2	216.6

4.2. Impact of modeling assumptions and closure models

4.2.1. Computational domain relevance

The role of upstream and downstream gaseous regions to the two-phase reactor region ($0 \leq x \leq L_{react}$ — see Fig. 1) is herein analyzed. In the literature related to the current field, there are a large number of works applying a similar mathematical model — governing equations and boundary conditions (at least stated as so) — that have neglected these regions. Therefore, for the numerical performance prediction of solar thermochemical reactors (and volumetric solar absorbers) besides neglecting upstream (entry) and downstream (exit) regions, the following assumptions are commonly considered in the literature (as they are in this work): (i) fluid flow governing equations (momentum, energy, and species balance equations) accounting for diffusive transport mechanisms; and (ii) constant (uniform along the radial direction) inlet first-type (Dirichlet) and zero outlet second-type (Neumann) boundary conditions for fluid flow governing equations.

Figs. 11(a), (b), and (c) present axial temperature, reactants mole fraction, and products (H_2 and CO) mole fraction profiles, respectively, considering the lowest inlet gas velocity ($u_{in,1}$) for three different computational domains: (i) with no reactor upstream region (N-UR); (ii) with no reactor downstream region (N-DR); and (iii) with upstream and downstream regions (UDR). The parameters L_{upstr} and $L_{downstr}$ (see Fig. 1) are set to zero for cases N-UR and N-DR, respectively, while the remaining reactor geometric parameters are held constant and equal to the case UDR. Table 5 lists the reactor performance parameters for the three computational domains under consideration. In this table, the two inlet gas velocity values are considered for the cases N-UR and UDR. The parameter Ω_{th} (second parameter listed in Table 5) corresponds to a spurious (non-physical) relative power loss due to non-conservation of governing equations at the inlet section — diffusive species and heat fluxes neglected at the inlet section due to the application of Dirichlet boundary conditions. This parameter is calculated according to Eq. (61), where $P_{tot,abs}$ corresponds to the net radiative power absorbed by the reactor.

$$\Omega_{th} = 1 - \frac{\eta_{th} Q_0}{P_{tot,abs}} \quad (61)$$

Figs. 11(a)–(c) and Table 5 show no striking differences between cases UDR and N-DR — temperature and species mole fraction profiles are almost coincident. (This is also concluded for the highest inlet gas velocity — not shown.) Therefore, for the conditions under consideration, extending the fluid domain downstream the reactor is not of paramount importance for an accurate reactor performance prediction. This is due to the non-existence of backflow issues at the reactor outlet section — that could be promoted by strong non-uniform radial velocity profiles at the reactor exit section — and due to the fact that

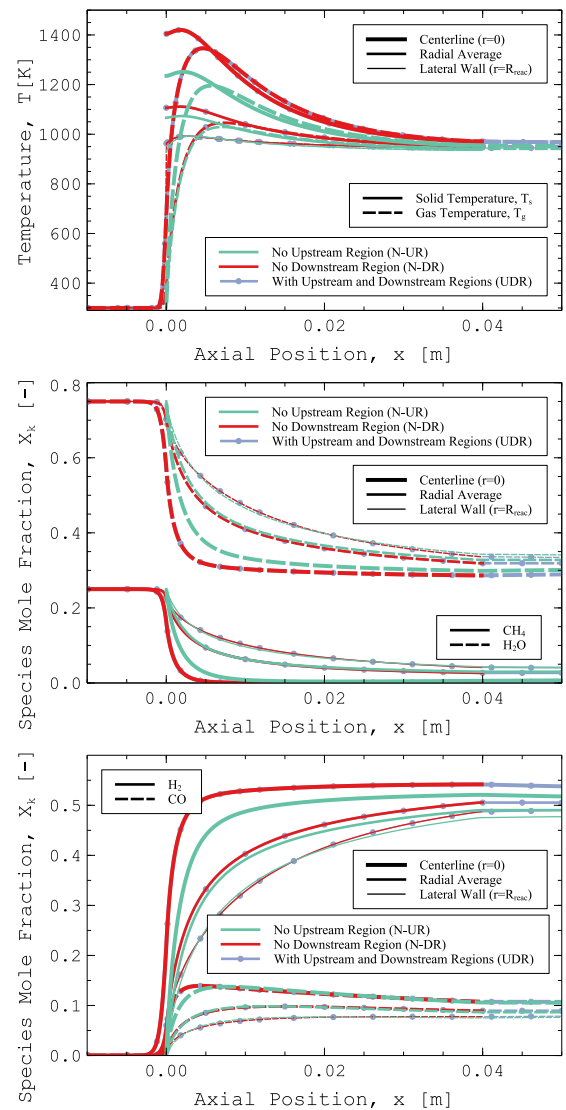


Fig. 11. Axial profiles of gas and solid temperatures (a), CH_4 and H_2O mole fractions (b), and H_2 and CO mole fractions (c) at the lowest inlet velocity for three different computational domains: (i) neglecting the reactor upstream region (no upstream region); (ii) neglecting the reactor downstream region (no downstream region); and (iii) considering both the upstream and downstream regions.

temperature and species mole fraction axial gradients are not very relevant near the reactor exit section.

On the other hand, neglecting the reactor upstream region (N-UR case) results in remarkable differences in relation to the results obtained with an entry length (or developing) region. Fig. 11(a) shows that significantly lower solid and gas temperatures are registered if the upstream region were not properly considered. The differences are more pronounced at the reactor centerline. For the lowest inlet gas velocity, the maximum solid (gas) temperature is underpredicted by about 169 K (151 K) if the upstream region is neglected. Figs. 11(b)–(c) also demonstrate a different performance, particularly at the centerline, where a higher (lower) mole fraction of reactants (products) is registered if the upstream region is neglected. Table 5 confirms that reactants conversion and products selectivity are lower for the N-UR case.

Lower solid temperatures observed for the case N-UR (in relation to the case UDR) would suggest a higher thermochemical efficiency since lower solid temperatures promote lower radiation emission losses. However, the contrary is observed — see Table 5. This apparent lack of

consistency is due to a non-negligible Ω_{th} value: for the lowest inlet gas velocity, about 3.1% of the net radiative power absorbed by the solid matrix is missing in the overall energy balance due to the application of inconsistent inlet boundary conditions (see Table 5) — or, alternatively, due to the application of an inappropriate computational domain for such type of boundary conditions. This (non-physical) power loss decreases as the inlet velocity increases — for the highest inlet gas velocity ($u_{in,2}$) considered Ω_{th} is approximately equal to 0.9% (see Table 5) — since diffusive transport is less relevant than the advective transport mechanism. This suggests that Dirichlet boundary conditions become less inadequate for accurate and physically consistent numerical predictions as the inlet gas velocity increases.

The application of an upstream fluid region ensures that velocity, temperature, and species mass fraction gradients (diffusive transport rates) vanish at the computational domain inlet section. (Note that in the vicinity of the reactor inlet section very high gas temperature and species mass fraction gradients establish.) Negligible gradients for solved scalars at the inlet section are fully compatible with the application of inlet first-type boundary conditions to the governing equations featuring diffusive transport mechanisms in order to ensure mass and energy conservation. The length of the upstream region (L_{upstr}) considered for cases UDR a N-DR (equal to 0.01 m) reveals to be sufficient to ensure negligible gradients at the inlet section — see Figs. 11(a)–(c) — and, consequently, full agreement with the conservation of energy principle applied to the overall reactor is achieved as concluded by a negligible Ω_{th} value in Table 5. (An alternative procedure to applying an upstream fluid region and still ensuring conservation of physical principles with governing equations featuring diffusive transport mechanisms consists in the application of the well-known Danckwerts boundary conditions — see Refs. [53,100].)

Even applying conservative inlet boundary conditions, the application of an upstream reactor region still benefits the reliability and accuracy of numerical predictions, particular, for multi-dimensional reactor models. This is due to the fact that a significantly different reactor operation along the radial direction — driven, for instance, by a highly non-uniform radial incident solar flux distribution or by the boundary layer development on the reactor outer wall — may lead the upstream flow to deviate from particular reactor regions which is perceived at the reactor front section by non-parallel flow streamlines. Numerical predictions carried out without an upstream region (even fully conservative) will hardly take into account such preferential (low resistance) flow paths at the reactor front section into the reactor performance.

Therefore, the differences registered between the cases N-UR and UDR are the cumulative outcome of unsuitable (non-conservative) boundary conditions and bi-dimensional reactor operation. Figs. 12(a), (b), and (c) present radial profiles for velocity components, species mole fractions, and gas and solid temperatures, respectively, at two reactor axial positions ($x = 0$ and $x = 0.01$ m) and for the three computational domains (N-UR, N-DR, and UDR). Again, no remarkable differences are observed between cases N-DR and UDR. On the other hand, significant differences are observed between cases N-UR and UDR, particularly at the reactor entrance. While constant (radially uniform) Dirichlet boundary conditions are applied for the case N-UR, Figs. 12(a)–(c) show that the application of an entry length allows the upstream flow conditions to take into account the conditions existing at the reactor. Therefore, non-uniform profiles at the reactor entrance section arise if a multi-dimensional reactor operation is established and an upstream region is considered. The non-uniform profile for the radial velocity component obtained for the case UDR at the reactor entrance section (see Fig. 12(a)) denounces that the streamlines are not parallel to each other and neither aligned with the x direction. Moreover, due to the non-uniform radial solar heat flux distribution, higher temperatures are observed near the centerline, and consequently, higher reaction rates and lower (higher) reactants (products) mole fractions. For the case N-UR this is only noticed at $x > 0$ — because at $x = 0$ the values for the dependent variables are prescribed — while for the case UDR this is perceived well upstream the reactor inlet section — in particular, at $x = 0$ as shown in Figs. 12(b)–(c).

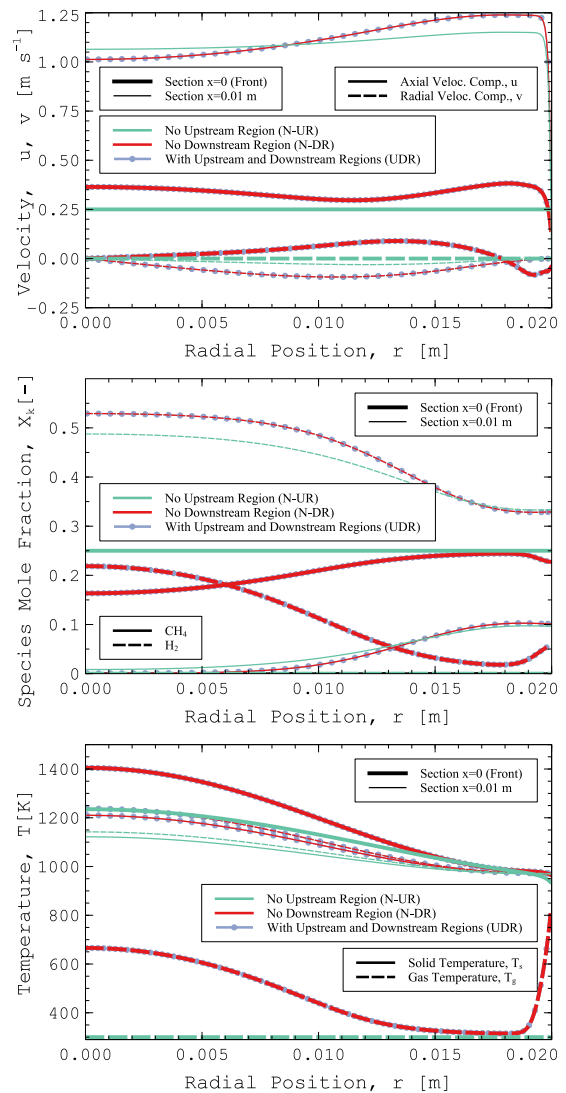


Fig. 12. Radial profiles of axial and radial velocity (a), CH₄ and H₂ mole fractions (b), and solid and gas temperatures (c) at the lowest inlet velocity for three different computational domains at two cross sections ($x = 0$ and $x = 0.01$ m).

4.2.2. Importance of species and gas-phase thermal diffusion

The relevance of species mass and gas-phase thermal (heat) diffusion transport mechanisms is herein investigated. Two sets of results are compared: one set obtained by excluding the first term on the RHS of Eq. (4) and the first and second terms on the RHS of Eq. (7) — gas-phase diffusion transport mechanisms neglected; and the other set including such terms — gas-phase diffusion transport mechanisms considered.

Figs. 13(a), (b), and (c) present axial temperature, reactants mole fraction, and products (H₂ and CO) mole fraction profiles, respectively, considering the lowest inlet gas velocity for both sets of results (neglecting and accounting for gas-phase diffusion transport mechanisms). Table 6 lists the corresponding reactor performance parameters calculated for the two inlet gas velocities considered in Table 2. Figs. 13(a)–(c) show that the most notable differences are observed near the reactor front section where high species mass fraction and temperature gradients establish. Neglecting diffusion, higher gas temperatures are observed, in particular, at the reactor centerline, where diffusion transport mechanisms take more relevance in relation to advective transport mechanisms — the maximum gas temperature increases by about 86 K neglecting diffusion. Neglecting diffusion transport rates, the position

Table 6

Performance parameters computed considering and neglecting species mass and gas-phase thermal diffusion transport mechanisms for two operating conditions — see Table 2.

Parameter	Gas-phase diffusion transport mechanisms			
	Neglecting		Accounting	
	$u_{in,1}$	$u_{in,2}$	$u_{in,1}$	$u_{in,2}$
η_{th} [%]	76.9	81.2	77.3	81.3
η_{chem} [%]	43.1	29.8	43.5	29.7
χ_{CH_4} [%]	84.0	30.6	84.7	30.6
χ_{H_2O} [%]	39.2	16.9	39.5	17.0
S_{H_2} [%]	61.0	31.0	61.3	31.1
S_{CO} [%]	59.9	34.8	60.2	33.2
H_2/CO [-]	5.7	10.5	5.6	11.0
$T_{s,max}$ [K]	1462.8	1174.7	1420.0	1174.6
$T_{s,avg}$ [K]	1010.6	885.8	1004.6	886.6
$T_{g,out}^{avg}$ [K]	952.9	854.2	951.7	856.5
Δp [Pa]	162.9	215.2	163.2	216.6

at the centerline where the maximum gas temperature is registered has equal gas and solid temperatures as required by Eq. (7). Higher gas temperatures lead to higher solid temperatures — the maximum solid temperature increase is about 43 K which is lower than the maximum gas temperature increase. However, such increase of solid temperatures near the reactor inlet section (observed while neglecting diffusion) does not lead to significantly higher radiative heat losses, as concluded by the corresponding thermochemical efficiency values in Table 6. If species diffusion is neglected in the model formulation, steep species mole fraction profiles are observed at the reactor entrance section — see Figs. 13(b)–(c). At the reactor inlet section, higher reactants and lower products mole fraction values are observed neglecting diffusion in relation to the results obtained with a mathematical model featuring species diffusion transport. At the centerline and towards the reactor exit section, higher reactants conversion and H_2 mole fraction values are observed due to higher solid temperatures and due to the absence of species diffusion. In terms of radial average axial profiles, both modeling approaches predict a similar performance — even though the results obtained with diffusion transport mechanisms are slightly superior (reactants conversion and syngas selectivity) — as anticipated by the results presented in Table 6. Neglecting diffusion transport and at the reactor lateral wall, the reactants (products) mole fraction values are lower (higher) than the radial average values. This evidence is generally not observed while considering diffusion transport mechanisms. This is observed because near the wall the advective transport mechanism (the sole transport mechanism if diffusion were neglected) is strongly limited and heat conduction from the lateral wall to the solid phase promotes high reaction rates that are unmatched with the transport rates from such location.

Table 6 shows that independently of the operating condition, the values for the first five integral reactor performance parameters predicted neglecting diffusion transport rates are generally slightly lower than the values for the corresponding parameters obtained accounting for diffusion. Moreover, an increase in the inlet gas velocity promotes a general approximation of such parameter values predicted neglecting diffusion to the values predicted considering diffusion. This evidence suggests that diffusion transport mechanisms become less relevant at higher inlet gas velocities. The slightly lower reactants conversion observed while neglecting diffusion is due to the absence of such transport mechanism to assist in the replacement of reaction products by fresh reactants in the regions where high temperatures promote high reaction rates. At the highest inlet gas velocity, the absence of transport rates by diffusion plays a particular role in the total oxidation of CO — production rates of CO_2 become limited due to excessive amounts of H_2 in relation to H_2O in the regions of highest temperatures. As a consequence, CO selectivity (H_2/CO ratio) predicted neglecting diffusion is slightly higher (lower) than considering diffusion.

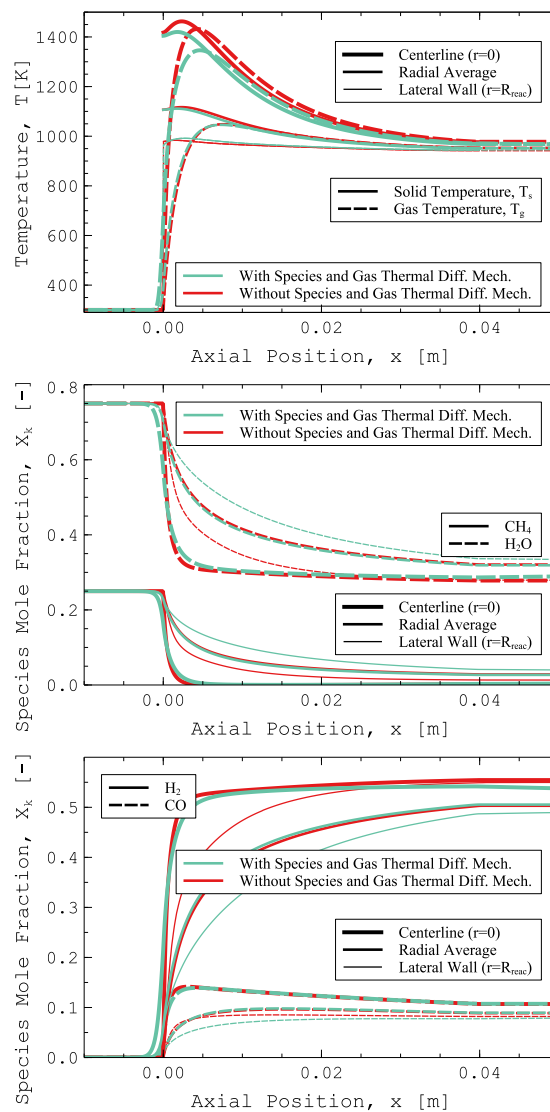


Fig. 13. Axial profiles of gas and solid temperatures (a), CH_4 and H_2O mole fractions (b), and H_2 and CO mole fractions (c) at the lowest inlet velocity, neglecting and accounting for species mass and gas-phase thermal diffusion transport mechanisms.

4.2.3. Reaction heat accounting on energy balance equations

In this section, two different procedures to account for the thermal effects due to chemical reactions (reaction heat) in the energy balance equations are considered. Results obtained with the procedure described in Section 3.1.3 — according to which the reaction heat is assigned to the solid-phase energy balance equation — are herein compared with results computed neglecting the source term S_{chem} (reaction heat) considered in gas- and solid-phase energy balance equations (Eqs. (7) and (12), respectively). According to the later procedure, the net heat consumption due to catalytic reactions is accounted for in the gas-phase energy balance equation. Additionally for the later procedure, surface net species production rates (\dot{s}_k) are calculated as a function of gas temperatures instead of solid temperatures in order to avoid decoupling issues between species mass and gas energy balance equations and to assure physically consistent and converged solutions — otherwise, the typically high solid temperatures observed near the reactor entrance section would lead to high species production/destruction rates which would cause a significant gas temperature drop therein unbalanced with the solid phase temperature since the convection heat transfer mechanism would be unable to provide the required power to the gas phase to compensate such a temperature

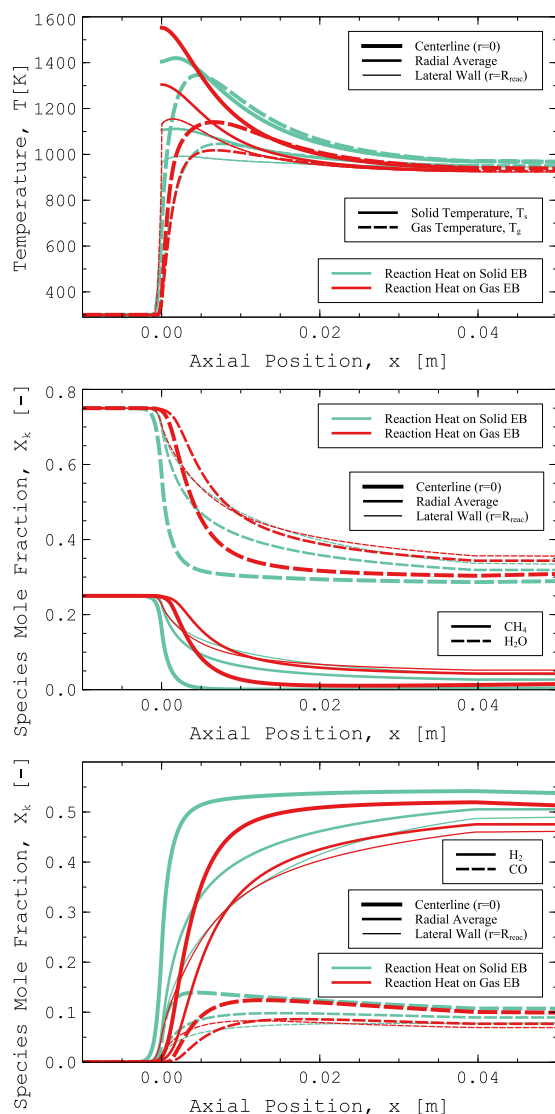


Fig. 14. Axial profiles of gas and solid temperatures (a), CH_4 and H_2O mole fractions (b), and H_2 and CO mole fractions (c) for two procedures to accounting for the reaction heat on the energy balance equations.

drop. Considering these two assumptions — reaction heat accounted for in the gas-phase energy balance equation and species production rates computed with the gas temperature —, the resulting mathematical model becomes similar to the models that have been widely applied in the literature on concentrated solar catalytic reforming. (The results computed with these assumptions are herein referred to as “reaction heat on gas EB” results, while those computed with the procedure described in Section 3.1 are labeled as “reaction heat on solid EB”).

Figs. 14(a), (b), and (c) present axial temperature, reactants mole fraction, and products (H_2 and CO) mole fraction profiles, respectively, considering the lowest inlet gas velocity for the two schemes under consideration: (i) reaction heat accounted for in the solid-phase energy balance equation; and (ii) reaction heat accounted for in the gas-phase energy balance equation. Table 7 lists the corresponding reactor performance parameters calculated for the two inlet gas velocities considered in Table 2. The results show remarkable differences applying these two approaches not only in terms of local performance but also considering the integral reactor thermochemical performance. Particularly, Fig. 14(a) shows that the gas and solid temperature profiles are more decoupled (temperature differences between phases are higher)

Table 7

Performance parameters computed considering two procedures to accounting for the reaction heat and for two operating conditions — see Table 2.

Parameter	Reaction heat accounting			
	Gas-phase energy balance		Solid-phase energy balance	
	$u_{in,1}$	$u_{in,2}$	$u_{in,1}$	$u_{in,2}$
η_{th} [%]	70.8	77.0	77.3	81.3
η_{chem} [%]	38.8	25.9	43.5	29.7
X_{CH_4} [%]	76.3	27.0	84.7	30.6
$X_{\text{H}_2\text{O}}$ [%]	36.7	15.5	39.5	17.0
S_{H_2} [%]	58.0	28.4	61.3	31.1
S_{CO} [%]	55.7	28.3	60.2	33.2
H_2/CO [-]	6.2	13.1	5.6	11.0
$T_{s,max}$ [K]	1552.4	1407.5	1420.0	1174.6
T_s^{avg} [K]	1017.2	920.0	1004.6	886.6
$T_{g,out}^{avg}$ [K]	926.9	855.0	951.7	856.5
Δp [Pa]	147.4	213.7	163.2	216.6

assigning the reaction heat to the gas-phase energy balance than to the solid-phase energy balance. Higher solid temperatures near the reactor front section are observed while considering the reaction heat accounted for in the gas-phase energy balance which are responsible for higher power losses — see in Table 7 the corresponding thermochemical efficiency values (70.8% vs. 77.3% for $u_{in,1}$). (Similar temperature profiles to those herein obtained considering the reaction heat assigned to the gas-phase energy balance (see Fig. 14(a)) have been reported elsewhere [15,60].) Figs. 14(b)–(c) show that reactants (products) generally present a local higher (lower) mole fraction value considering the reaction heat assigned to the gas-phase energy balance than to the solid-phase energy balance. This evidence is observed because considering the reaction heat assigned to the gas-phase energy balance, the species production/destruction rates are lower once the temperatures at which the kinetic rates are evaluated (gas temperature values) are also lower.

For the two different inlet gas velocity values, Table 7 shows significantly lower values for efficiency, reactants conversion, and H_2 and CO selectivities by considering the reaction heat assigned to the gas-phase energy balance than to the solid-phase energy balance. (Only the H_2/CO ratio is enhanced since a preferential net production of H_2 in relation to the net production of CO is observed at lower reaction temperatures.) For the highest inlet gas velocity, differences between the two approaches are still meaningful but generally in a lower extent in comparison to the values registered for the lowest inlet gas velocity. An increase in the inlet gas velocity promotes a decrease in the maximum and average solid temperatures. However, such a temperature decrease is more striking for the case that considers the reaction heat accounted for in the solid-phase energy balance due to the thermal role (heat consumption) of reactions that for this case are observed in a higher extent than for the alternative procedure.

Assigning the reaction heat to the gas-phase energy balance — and computing species production rates at the gas-phase temperature — introduce an additional thermal resistance (due to finite convection heat transfer coefficients) between the concentrated solar power and the reactor phase where the reactions are accounted for (modeled). Operating conditions that promote a decrease of such additional thermal resistance, namely increasing the inlet gas velocity, lead the results obtained assigning the reaction heat to the gas-phase energy balance to approximate the results computed considering the reaction heat accounted for in the solid-phase energy balance.

Assigning the reaction heat to the gas-phase energy balance equation results in strong underpredictions for the reactor thermochemical efficiency and reforming performance that increase for lower inlet gas velocities.

4.2.4. Local thermal equilibrium (LTE) vs. local thermal non-equilibrium (LTNE) models

In this section, a comparison between two approaches for modeling the reactor energy balance (LTNE vs. LTE) is considered. The LTNE

Table 8

Performance parameters computed considering the LTNE and LTE reactor energy models for two operating conditions — see Table 2.

Parameter	Energy model			
	LTE model		LTNE model	
	$u_{in,1}$	$u_{in,2}$	$u_{in,1}$	$u_{in,2}$
η_{th} [%]	78.6	82.9	77.3	81.3
η_{chem} [%]	44.5	30.9	43.5	29.7
X_{CH_4} [%]	86.5	31.7	84.7	30.6
X_{H_2O} [%]	40.0	17.5	39.5	17.0
S_{H_2} [%]	61.9	31.9	61.3	31.1
S_{CO} [%]	61.3	34.5	60.2	33.2
H_2/CO [-]	5.5	10.6	5.6	11.0
$T_{s,max}$ [K]	1383.3	1121.6	1420.0	1174.6
T_s^{avg} [K]	1007.0	887.3	1004.6	886.6
$T_{g,out}^{avg}$ [K]	955.3	859.4	951.7	856.5
Δp [Pa]	171.1	231.6	163.2	216.6

model details are thoroughly described in Section 3.1.3. The LTE model assumes that both phases are at the same temperature at every reactor local position. Consequently, the set of two equations required for the LTNE model is replaced by only one energy balance equation for the LTE model. This equation is obtained by equating the sum of the LHS terms of Eqs. (7) and (12) to the sum of the RHS terms of the same equations and stating $T \equiv T_g = T_s$. Accordingly, the interphase (convection) heat transfer term and reaction heat source term (S_{chem}) vanish and the overall (effective) thermal conductivity is given by $\lambda_{eff} = \lambda_{g,eff} + \lambda_{s,eff}$, where the $\lambda_{g,eff}$ and $\lambda_{s,eff}$ are computed considering Eqs. (8) and (13), respectively. The corresponding boundary condition at the reactor lateral wall is obtained applying a similar procedure to Eq. (48).

Figs. 15(a), (b), and (c) present axial temperature, reactants mole fraction, and products (H_2 and CO) mole fraction profiles, respectively, considering the lowest inlet gas velocity for the LTNE and LTE models. Table 8 lists the reactor performance parameters obtained with the two energy models under consideration. Fig. 15(a) shows that centerline and radial average temperature profiles predicted by the LTE model along the first few millimeters of the reactor are in between the gas and solid temperature profiles predicted by the LTNE model for the centerline and radial average, respectively. Lower radiative heat losses are calculated considering the LTE model since the corresponding temperatures — that are applied to evaluate the rates of radiative heat transfer — are lower than the solid temperatures predicted by the LTNE model, particularly, near the reactor front section. Therefore, higher values for thermochemical efficiency are observed for the LTE than for the LTNE model — see Table 8. Figs. 15(b)–(c) present minor differences between both modeling approaches. A slightly superior integral reforming performance is registered for the LTE model — higher chemical efficiency, reactants conversion, and H_2 and CO selectivity (see Table 8).

Note that the results obtained considering the LTE model can also be compared with those predicted with the LTNE model considering the reaction heat accounted for in the gas-phase energy balance — set of results presented in Section 4.2.3. This is because when interphase or external (convection) heat transfer resistance is negligible (LTE model is suitable), the phase into which the net thermal effect from chemical reactions is accounted for becomes irrelevant. The comparison between these two sets of results (LTE model and LTNE model with reaction heat accounted for in the gas-phase energy balance) — see Figs. 14(a)–(c) and 15(a)–(c) and Tables 7 and 8 — shows remarkable differences. For instance, considering the lowest inlet gas velocity, the thermochemical efficiency predicted by the LTE model and LTNE model with reaction heat assigned to the gas-phase energy balance is equal to 78.6% and 70.8%, respectively.

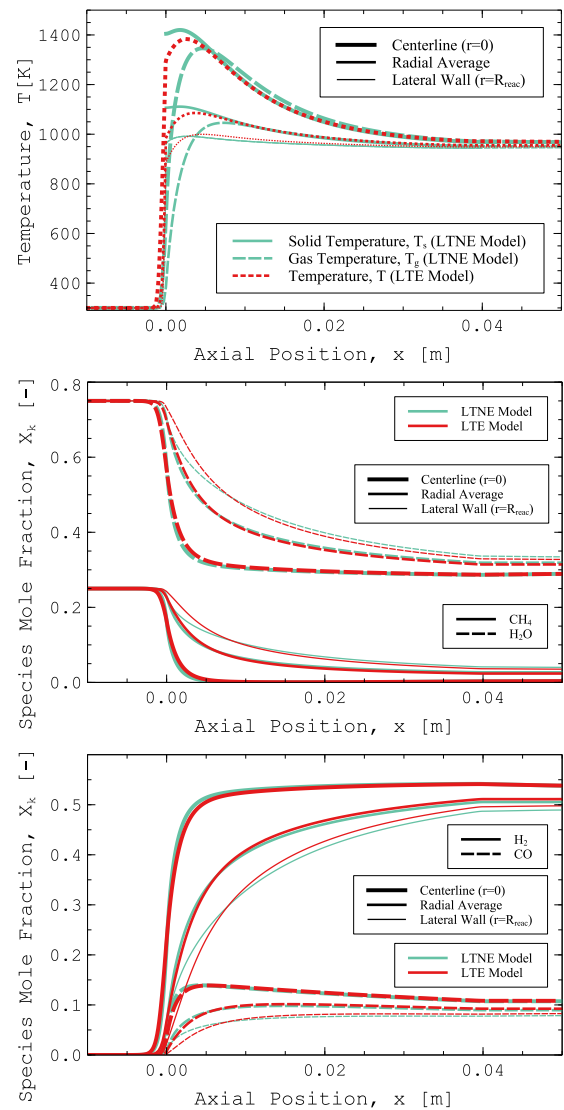


Fig. 15. Axial profiles of gas and solid temperatures (a), CH_4 and H_2O mole fractions (b), and H_2 and CO mole fractions (c) at the lowest inlet velocity for the LTNE and LTE reactor energy models.

4.2.5. Model dimension: 1D vs. 2D models

In this section the relevance of velocity, temperature, and species mass fraction gradients along the radial coordinate of the reactor is investigated. Results computed considering the 2D model are compared with results predicted by a 1D model (distributed model exclusively along the axial direction). For ease of solution computation, the same computational domain considered for the 2D model was applied to obtain 1D numerical solutions. The only differences between both models rely on the boundary conditions applied at the lateral wall ($r = R$) and the concentrated solar heat flux value. At the reactor lateral wall, the 1D model assumes negligible radial gradients for the solved variables (zero-Neumann) and slip boundary conditions. The concentrated solar heat flux distribution is uniform (constant) for the 1D model. Three different concentrated solar heat flux (q''_0) values are considered for the 1D model: (i) the value computed with the parameters A and B (see Table 2) in Eq. (17) at the lateral wall ($q''_{0,1} \approx 538.73 \text{ kW m}^{-2}$); (ii) the radial average value considering the stated parameters and equation ($q''_{0,2} \approx 938.74 \text{ kW m}^{-2}$); and (iii) the value computed with the stated parameters and equation at the reactor centerline ($q''_{0,3} = 1500.00 \text{ kW m}^{-2}$). Case (ii) is the most representative case for the actual 2D problem. The remaining cases are herein considered to compare the

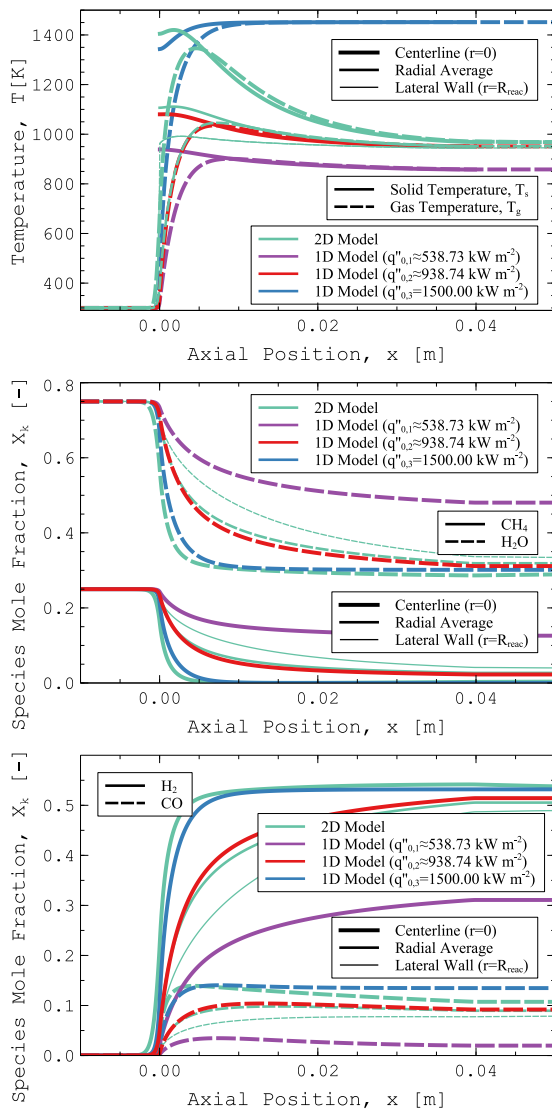


Fig. 16. Axial profiles of gas and solid temperatures (a), CH₄ and H₂O mole fractions (b), and H₂ and CO mole fractions (c) at the lowest inlet velocity for the 2D model and for the 1D model considering three different values for the concentrated solar heat flux at the reactor front section.

corresponding 1D model results with the 2D model results at the lateral wall and centerline — Cases (i) and (iii), respectively.

Figs. 16(a), (b), and (c) present axial temperature, reactants mole fraction, and products (H₂ and CO) mole fraction profiles, respectively, considering the lowest inlet gas velocity for the 1D and 2D models. Table 9 lists the reactor performance parameters obtained with the 1D and 2D models. Fig. 16(a) shows that the 1D model featured with the average value for the concentrated solar heat flux ($q''_{0,2}$) predicts slightly lower solid and gas temperatures along the reactor in comparison with the radial average profiles along the axial direction computed with the 2D model. The lower solid temperatures observed for the 1D model are in agreement with the higher thermochemical efficiency presented in Table 9. The 1D model predicts higher chemical efficiency, conversion of reactants, and H₂ and CO selectivity values than the 2D model — see Table 9. However, the 1D model is unable to predict the large range of temperatures and species mole fractions between the centerline and the lateral wall for the same reactor axial position, which is particularly relevant near the reactor entrance section — see Figs. 16(a)–(c).

For the highest inlet gas velocity ($u_{in,2}$), Table 9 shows similar values for the thermochemical efficiency obtained by both models. For

Table 9

Performance parameters computed considering the 1D and 2D models for two operating conditions — see Table 2.

Parameter	Model dimension					
	1D			2D		
	$q''_{0,1}$	$q''_{0,2}$	$q''_{0,3}$	$q''_{0,1}$	$q''_{0,2}$	$q''_{0,3}$
	$u_{in,1}$	$u_{in,1}$	$u_{in,2}$	$u_{in,1}$	$u_{in,1}$	$u_{in,2}$
η_{th} [%]	78.7	78.6	81.2	73.5	77.3	81.3
η_{chem} [%]	32.7	44.7	29.2	33.6	43.5	29.7
χ_{CH_4} [%]	39.6	87.0	30.6	100.0	84.7	30.6
χ_{H_2O} [%]	23.2	40.4	17.6	39.7	39.5	17.0
S _{H₂} [%]	39.3	62.3	31.5	63.8	61.3	31.1
S _{CO} [%]	24.0	60.7	27.5	80.9	60.2	33.2
H ₂ /CO [-]	15.7	5.6	13.6	3.9	5.6	11.0
T _{s,max} [K]	938.7	1080.5	978.8	1451.6	1420.0	1174.6
T _{s,avg} [K]	882.9	989.8	886.5	1443.4	1004.6	886.6
T _{g,out} [K]	858.0	950.9	859.7	1451.5	951.7	856.5
Δp [Pa]	107.0	160.6	214.6	340.1	163.2	216.6

this operating condition, the 1D solid temperature profile is almost coincident with the radial average solid temperature profile for the 2D model with a maximum absolute difference of about 6 K — not shown. (See the temperature profiles predicted by the 2D model for this operating condition in Fig. 7(b).) With an increase in the inlet gas velocity, the differences for the values of reactants conversion and H₂ selectivity between both models generally decrease. An exception is observed for the CO selectivity whose difference between model approaches is increased by increasing the inlet gas velocity from 0.25 to 0.50 m s⁻¹. For high inlet gas velocities, CO selectivities predicted by the 1D model are clearly lower than the values predicted by the 2D model — this was also observed for higher inlet gas velocities, particularly for 0.75 and 1.00 m s⁻¹ (not shown). For high inlet gas velocities, the preferential production of CO₂ rather than CO observed for the 1D model in relation to the performance of the 2D model is due to the lower temperatures obtained by the 1D model in relation to local higher temperatures along the radial direction computed with the 2D model. Consequently, for high inlet gas velocity values, the ratio H₂/CO is overpredicted by considering the 1D model.

Considering the 1D model applied with the lowest concentrated solar heat flux value ($q''_{0,1}$), lower temperatures and products mole fractions than those observed with the 2D model at the lateral wall are registered — see Figs. 16(a) and (c). Therefore, although both models (1D and 2D model at the lateral wall) take into account an equal concentrated solar heat flux value, the 2D model at the lateral wall presents better reforming performance (lower reactants and higher products mole fractions) due to the net radiative and conduction heat gains from the interior of the reactor.

The 1D model applied for the highest concentrated solar heat flux value ($q''_{0,3}$) presents lower solid temperatures near the reactor front section and higher solid temperatures downstream in comparison with the 2D model solid temperatures at the reactor centerline — see Fig. 16(a). Since the irradiation heat flux is equal for both cases (1D model applied with $q''_{0,1}$ and 2D model at the reactor centerline), lower solid temperatures should be observed for the 2D model due to radial net radiative heat losses and conduction heat transfer from the reactor centerline once such mechanisms are not available in the 1D model. However, this is not observed near the reactor entrance section because for the 2D model the axial velocity component, mixture composition, and temperature are not uniform along the radial direction at the reactor entrance section — see Figs. 12(a)–(c) —, whereas for the 1D model, radial gradients are intrinsically absent. Particularly, near the reactor front section and at the centerline, the velocity magnitude for the 2D model is slightly lower than for the 1D model. Consequently, local convection heat transfer coefficients are lower in this region for the 2D model than for the 1D model, the solid phase has a higher

resistance to transfer heat to the gas phase, and ultimately, its steady-state temperature increases. This higher convection thermal resistance observed in the 2D model in comparison with the 1D model near the reactor entrance and at the centerline justifies the higher solid temperatures observed for the 2D model.

The 1D model applied with $q''_{0,1}$ and $q''_{0,3}$ strongly underpredicts and overpredicts, respectively, temperatures, reactants conversion, H_2 and CO selectivity values — see Table 9. The ratio H_2/CO is overpredicted considering $q''_{0,1}$ and underpredicted considering $q''_{0,3}$. The chemical efficiency obtained for $q''_{0,1}$ and $q''_{0,3}$ is lower than the actual 2D value.

4.2.6. Convection heat transfer correlations

The reactor performance predicted taking into account two different correlations for the local volumetric convection heat transfer coefficient is herein presented and compared. These two correlations were developed by: (i) Xia et al. [32] (see Eq. (9)); and (ii) Wu et al. [101] (see Eq. (62), where $Re \equiv \rho_g |\mathbf{u}| d_c / \mu_g$). The later correlation was developed through pore-scale numerical simulations with simplified (idealized) foam geometrical models along the ranges $0.66 < \phi < 0.93$ and $70 < Re < 800$. This correlation has been extensively applied in the literature [9,11,14].

$$h_v = \frac{\lambda_g Re^{0.438}}{d_c^2} (32.504\phi^{0.38} - 109.94\phi^{1.38} + 166.65\phi^{2.38} - 86.98\phi^{3.38}) \quad (62)$$

Both correlations were developed for open-cell foam structures and are widely applied for concentrated solar energy applications. (This study could have embraced more correlations such as those considered in Refs. [14,31–33]. However, some of such additional correlations were not developed for open-cell foam structures under concentrated solar energy conditions and have a marginal application relevance in literature of the current topic.)

Figs. 17(a), (b), and (c) present axial temperature profiles, axial CH_4 and H_2 mole fraction profiles, and axial and radial profiles for the volumetric convection heat transfer coefficient, respectively, predicted according to the two correlations under consideration for the lowest inlet gas velocity. Table 10 lists the corresponding reactor performance parameters computed for the two inlet gas velocities defined in Table 2. Fig. 17(a) shows that near the reactor entrance section the correlation reported by Wu et al. predicts simultaneously lower solid temperatures and, more strikingly, higher gas temperatures — and, consequently, lower temperature differences between phases — than the correlation reported by Xia et al. This is due to the fact that the correlation proposed by Wu et al. provides higher values for the volumetric convection heat transfer coefficient than the correlation proposed by Xia et al. — see Fig. 17(c). (The order of magnitude for the values presented in Fig. 17(c) are in agreement with the literature [14].) At the reactor centerline, the average volumetric convection heat transfer coefficients predicted with the correlations by Wu et al. and Xia et al. are about 1.07×10^6 and $0.29 \times 10^6 \text{ W m}^{-3} \text{ K}^{-1}$, respectively. Considering the porous structure specific surface area (see Table 1), the stated average volumetric convection heat transfer coefficients correspond to about 453.39 and 122.88 $\text{W m}^{-2} \text{ K}^{-1}$ in terms of (surface) convection heat transfer coefficients ($h \equiv h_v/a_v$). The average h value predicted with the correlation developed by Xia et al. is well within the typical range for gases under the forced convection regime (25 – 250 $\text{W m}^{-2} \text{ K}^{-1}$), whereas the value calculated with the correlation proposed by Wu et al. is somewhat above such range.

Along the first few millimeters of the reactor and considering the correlation by Wu et al., more power is transferred from the solid matrix to the gas-phase mixture, and consequently, less power is available for driving chemical reactions (taking place at the solid-phase surface) and feeding radiative heat losses. Note that considering the correlation by Wu et al., lower rates of species consumption/production are observed and concluded by slightly lower (higher) values for H_2 (CH_4) mole fractions observed near the reactor entrance section — see

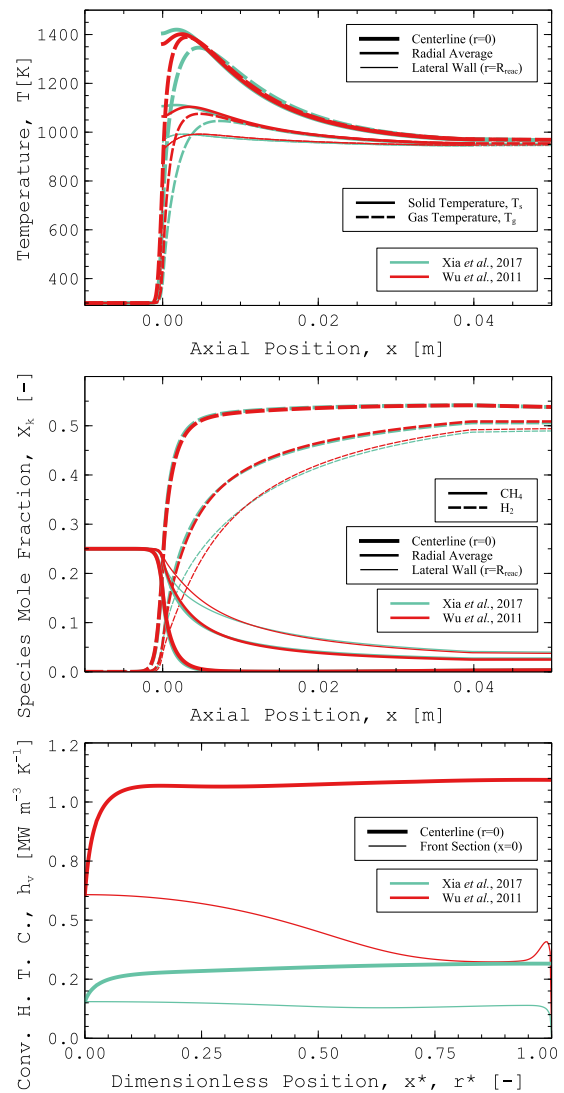


Fig. 17. Axial profiles of gas and solid temperatures (a) and CH_4 and H_2 mole fractions (b), and axial and radial profiles for the volumetric convection heat transfer coefficient at the reactor centerline and front section, respectively (c) at the lowest inlet velocity computed with the correlations reported by Wu et al., 2011 [101] and Xia et al., 2017 [32].

Table 10

Performance parameters computed considering two different correlations for the volumetric convection heat transfer coefficient and for two operating conditions — see Table 2.

Parameter	Convection heat transfer correlation			
	Wu et al., 2011 [101]		Xia et al., 2017 [32]	
	$u_{in,1}$	$u_{in,2}$	$u_{in,1}$	$u_{in,2}$
η_{th} [%]	78.0	82.1	77.3	81.3
η_{chem} [%]	44.1	30.3	43.5	29.7
X_{CH_4} [%]	85.7	31.2	84.7	30.6
X_{H_2O} [%]	39.8	17.2	39.5	17.0
S_{H_2} [%]	61.7	31.5	61.3	31.1
S_{CO} [%]	60.8	34.4	60.2	33.2
H_2/CO [-]	5.6	10.6	5.6	11.0
$T_{s,max}$ [K]	1401.6	1135.8	1420.0	1174.6
T_s^{avg} [K]	1006.8	887.9	1004.6	886.6
$T_{g,out}^{avg}$ [K]	953.8	858.4	951.7	856.5
Δp [Pa]	168.0	224.9	163.2	216.6

Fig. 17(b). In addition, note that lower radiative heat losses (lower solid temperatures) are in line with the higher thermochemical efficiency

values predicted while applying the correlation reported by Wu et al. — see Table 10. Downstream the reactor entrance section, the power transferred to the gas mixture along the first few millimeters of the reactor is transferred back to the solid phase to promote chemical reactions. Although this heat exchange mechanism is observed independently of the applied correlation, this power contribution is much more relevant for the correlation reported by Wu et al., which justifies the overtake observed by the radial average mole fraction profiles obtained with this correlations at about 0.08 m (see Fig. 17(b)), and the higher values observed in Table 10 for chemical efficiency, reactants conversions, and syngas selectivities. (This heat exchange mechanism is generally not observed considering the reaction heat accounted for in the gas-phase energy balance since the radial-averaged gas-phase temperature is always below the radial-averaged solid-phase temperature — see Fig. 14(a).)

If the gas-phase temperature were considered to compute the surface reaction rates, higher reaction rates would be expected near the reactor entrance section considering the correlation suggested by Wu et al. — since the gas temperatures are higher than those obtained with the correlation by Xia et al. — as well as higher thermochemical efficiency values. Similar conclusions have been observed in the literature [14].

The LTE approach becomes as suitable as the temperature difference between phases decreases which is observed as the volumetric convection heat transfer coefficients are increased — both phases truly achieve thermal equilibrium conditions for an infinite volumetric convection heat transfer coefficient. In the literature, LTE models — applied mainly to predict the performance of volumetric solar absorbers — have shown to predict lower radiative heat losses, and consequently, higher thermal efficiency values in comparison with LTNE models featuring suitable and finite convection heat transfer coefficients [34]. This is in agreement with the results herein presented: since the correlation by Wu et al. provides a higher thermal coupling level between phases than the correlation by Xia et al., the thermochemical efficiency is also higher — see Table 10.

Although local differences between the reactor performance applying both correlations are particularly relevant for gas temperatures and near the reactor entrance section, the differences are not significant at the reactor outlet section. This is due to the considered reactor length, to comparable radiative heat losses obtained with both correlations, and to the fact that surface kinetics is evaluated at local temperature values of the solid phase.

4.2.7. Effective solid thermal conductivity correlation

In this section, two correlations for the effective solid thermal conductivity are considered. Numerical model results computed with the correlation given by Eq. (13) (in this study referred to as Correlation 1) are compared with the results evaluated considering Eq. (63) (Correlation 2).

$$\lambda_{s,eff} = (1 - \phi) \lambda_s \quad (63)$$

These correlations have been applied in the literature for ceramic open-cell foams in concentrated solar power applications — see e.g. Refs. [15, 18,45,49,94,102–104] and [8,34,43,46,105] for works applying Correlation 1 and Correlation 2, respectively. Nevertheless, Correlation 1 has been the most preferred correlation.

Figs. 18(a), (b), and (c) present axial temperature, reactants mole fraction, and products (H₂ and CO) mole fraction profiles, respectively, considering the lowest inlet gas velocity for Correlations 1 and 2. Table 11 lists the reactor performance parameters obtained with the two correlations.

Fig. 18(a) shows that applying Correlation 2 lower centerline and average temperatures are observed in relation to the results computed with Correlation 1. Moreover, the range of temperatures is narrower (along the radial and axial directions) with Correlation 2 than with Correlation 1. Note that for a particular axial position, the highest

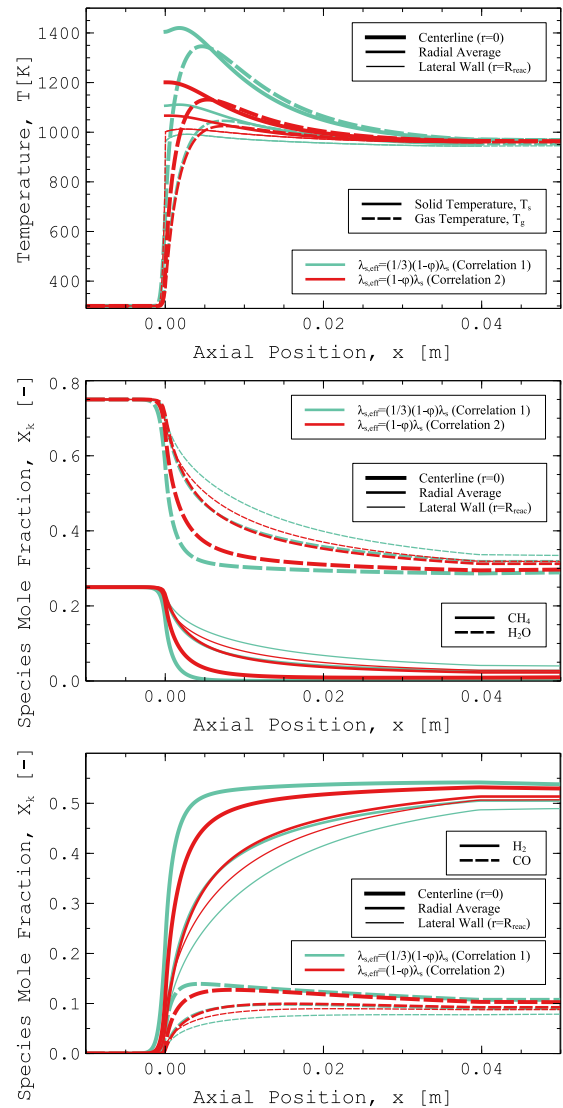


Fig. 18. Axial profiles of gas and solid temperatures (a), CH₄ and H₂O mole fractions (b), and H₂ and CO mole fractions (c) at the lowest inlet velocity predicted by different correlations for the effective solid thermal conductivity.

Table 11

Performance parameters computed considering different effective solid thermal conductivity correlations for two operating conditions — see Table 2.

Parameter	Effective solid thermal conductivity ($\lambda_{s,eff}$) correlation			
	$(1 - \phi) \lambda_s$ (Correlation 2)		$(1/3)(1 - \phi) \lambda_s$ (Correlation 1)	
	$u_{in,1}$	$u_{in,2}$	$u_{in,1}$	$u_{in,2}$
η_{th} [%]	79.1	81.8	77.3	81.3
η_{chem} [%]	44.7	29.5	43.5	29.7
X_{CH_4} [%]	86.9	30.6	84.7	30.6
X_{H_2O} [%]	40.2	17.3	39.5	17.0
S_{H_2} [%]	62.2	31.4	61.3	31.1
S_{CO} [%]	61.0	29.8	60.2	33.2
H ₂ /CO [-]	5.6	12.4	5.6	11.0
$T_{s,max}$ [K]	1201.1	1064.2	1420.0	1174.6
T_s^{avg} [K]	993.1	887.4	1004.6	886.6
$T_{g,out}^{avg}$ [K]	960.3	863.8	951.7	856.5
Δp [Pa]	161.6	216.4	163.2	216.6

and lowest temperatures are registered for the Correlation 1 — at the centerline and lateral wall, respectively. Since solid temperatures are lower for Correlation 2, radiative heat losses are also lower and thermochemical efficiency are higher in comparison with Correlation 1

— see Table 11. In Figs. 18(b)–(c), higher reaction rates are observed near the reactor entrance section for Correlation 1 by lower (higher) reactants (products) mole fraction values. However, due to the higher radiative losses acknowledged for Correlation 1 and to the considered length for the reactor, the reforming performance at the reactor outlet section is slightly better for Correlation 2 — see Table 11.

The comparison between the results obtained with these two correlations can also be seen as a comparison between two different values for the intrinsic solid thermal conductivity (λ_s) for the same correlation — *i.e.*, in Figs. 18(a)–(c) and Table 11, the results for Correlation 2 can be interpreted as results obtained with Correlation 1 with a three-fold increase in λ_s . Under such a perspective, the qualitative behavior for the reactor performance herein observed is generally in agreement with literature studies on the effect of solid thermal conductivity in concentrated solar volumetric absorbers [34,45,106] and reactors for methane steam reforming [19], methane dry reforming [15], and methane bi-reforming [10].

5. Conclusions

In the last decade, the performance of solar thermochemical reactors (and volumetric solar absorbers) has been predicted considering different model formulations and simplifying assumptions. In this work, widely applied modeling assumptions and closure models are compared for the prediction of solar-driven methane steam reforming in an open-cell foam reactor. A consistent set of governing equations and boundary conditions are provided in compliance with the volume-averaging approach. Particular discussions on conflicting modeling details applied in the literature are provided. Detailed surface reaction kinetics for methane steam reforming is considered. The model is successfully verified considering different benchmark results. The following conclusions can be drawn from this study:

- according to chemical equilibrium calculations, for the lowest inlet gas velocity considered ($u_{in,1}$) a reactor thermochemical efficiency in the range 81.6%–87.3% is required to observe the maximum values for H₂O conversion, H₂ selectivity, and η_{chem}/η_{th} ratio; for $2u_{in,1}$, these maximum values cannot even be achieved since a thermochemical efficiency higher than one would have to be considered;
- for the lowest inlet gas velocity, the detailed investigation on the reactor performance reveals a thermochemical efficiency approximately equal to 77.3% (for an inert porous structure this value would be equal to 59.3%); the most relevant power loss contribution occurs through the reactor front face; an increase in the inlet gas velocity promotes a decrease in power losses, and, consequently, an increase in the thermochemical efficiency, even though chemical efficiency decreases — the absorbed power is preferentially stored as sensible (thermal) energy;
- the computational domain should be extended upstream from the reactor inlet section to avoid two issues: (a) scalar non-conservation while applying inlet first-type boundary conditions to gas-phase governing equations featuring diffusive transport terms; and (b) inability to account for preferential flow paths at the inlet section promoted by a non-uniform downstream radial temperature distribution;
- neglecting species and gas-phase heat diffusion mechanisms results in slightly higher gas and solid maximum temperatures — particularly, for lower inlet gas velocities —, even though the corresponding radiative heat losses are not significantly increased;
- remarkable differences are observed while considering the reaction heat (net heat consumption due to catalytic reactions) accounted for in gas-phase or solid-phase energy balances; the reaction heat should be assigned to the solid-phase energy balance as it is commonly considered in the heterogeneous catalysis reactor modeling literature;

- lower radiative heat losses (higher thermochemical efficiencies) are predicted applying the local thermal equilibrium (LTE) approach in relation to the local thermal non-equilibrium (LTNE) approach; centerline and radial average temperature profiles along the axial direction predicted by LTE model are in between the corresponding solid and gas temperatures profiles predicted by the LTNE; LTE model results are strikingly different from the results obtained applying the LTNE model with the reaction heat accounted for in the gas-phase energy balance (class of models extensively applied for solar volumetric reforming reactors);
- a one-dimensional model provided with an average concentrated solar heat flux value is able to predict the reactor integral performance but unable to predict the large temperature and species mole fraction differences observed near the reactor inlet section along the radial direction;
- the correlation for local volumetric convection heat transfer coefficients suggested by Wu et al. provides higher values than the correlation developed by Xia et al.; consequently, solid- and gas-phase temperature differences are lower for the former correlation; convection heat transfer coefficients predicted with the empirical correlation by Xia et al. are within the typical range for forced convection regime whereas the values predicted by the Wu et al. correlation are relatively higher;
- two different effective solid thermal conductivity correlations commonly applied in the literature for open-cell foams predict a significantly different local reactor performance and slightly different integral performance, particularly for low inlet gas velocities.

The relevance of this work extends well beyond concentrated solar thermochemical applications since similar models and assumptions have also been broadly applied for predicting the performance of volumetric solar absorbers.

CRedit authorship contribution statement

Jorge E.P. Navalho: Conceptualization, Methodology, Software, Validation, Investigation, Writing – original draft, Writing – review & editing, Visualization. **José C.F. Pereira:** Resources, Writing – review & editing, Funding acquisition.

Declaration of competing interest

The authors declare that they have no known competing financial interests or personal relationships that could have appeared to influence the work reported in this paper.

Data availability

Data will be made available on request.

Acknowledgments

This work was supported by the Portuguese Foundation for Science and Technology (FCT), through IDMEC, under LAETA, project UIDB/50022/2020.

References

- [1] Capuano R, Fend T, Schwarzbözl P, Smirnova O, Stadler H, Hoffschmidt B, Pitz-Paal R. Numerical models of advanced ceramic absorbers for volumetric solar receivers. *Renew Sustain Energy Rev* 2016;58:656–65. <http://dx.doi.org/10.1016/j.rser.2015.12.068>, URL <https://www.sciencedirect.com/science/article/pii/S1364032115014513>.
- [2] Avila-Marin A, Fernandez-Reche J, Martinez-Tarifa A. Modelling strategies for porous structures as solar receivers in central receiver systems: A review. *Renew Sustain Energy Rev* 2019;111:15–33. <http://dx.doi.org/10.1016/j.rser.2019.03.059>, URL <https://www.sciencedirect.com/science/article/pii/S1364032119301996>.

- [3] He Y-L, Du S, Shen S. Advances in porous volumetric solar receivers and enhancement of volumetric absorption. *Energy Rev* 2023;2(3):100035. <http://dx.doi.org/10.1016/j.enrev.2023.100035>, URL <https://www.sciencedirect.com/science/article/pii/S2772970223000226>.
- [4] Ávila-Marín AL. Volumetric receivers in solar thermal power plants with central receiver system technology: A review. *Sol Energy* 2011;85(5):891–910. <http://dx.doi.org/10.1016/j.solener.2011.02.002>, URL <https://www.sciencedirect.com/science/article/pii/S0038092X11000302>.
- [5] Romero M, Steinfeld A. Concentrating solar thermal power and thermochemical fuels. *Energy Environ Sci* 2012;5(11):9234–45.
- [6] Behar O, Khellaf A, Mohammadi K. A review of studies on central receiver solar thermal power plants. *Renew Sustain Energy Rev* 2013;23:12–39. <http://dx.doi.org/10.1016/j.rser.2013.02.017>, URL <https://www.sciencedirect.com/science/article/pii/S1364032113001184>.
- [7] Carotenuto A, Reale F, Ruocco G, Nocera U, Bonomo F. Thermal behaviour of a multi-cavity volumetric solar receiver: Design and tests results. *Sol Energy* 1993;50(2):113–21. [http://dx.doi.org/10.1016/0038-092X\(93\)90082-Y](http://dx.doi.org/10.1016/0038-092X(93)90082-Y), URL <https://www.sciencedirect.com/science/article/pii/0038092X9390082Y>.
- [8] Pitz-Paal R, Hoffschmidt B, Böhmer M, Becker M. Experimental and numerical evaluation of the performance and flow stability of different types of open volumetric absorbers under non-homogeneous irradiation. *Sol Energy* 1997;60(3):135–50. [http://dx.doi.org/10.1016/S0038-092X\(97\)00007-8](http://dx.doi.org/10.1016/S0038-092X(97)00007-8), URL <https://www.sciencedirect.com/science/article/pii/S0038092X97000078>.
- [9] Chen X, Wang F, Yan X, Cheng Z, Han Y, Jie Z. Thermal and chemical analysis of methane dry reforming in a volumetric reactor under highly concentrated solar radiation. *Sol Energy* 2018;162:187–95. <http://dx.doi.org/10.1016/j.solener.2018.01.032>, URL <https://www.sciencedirect.com/science/article/pii/S0038092X18300537>.
- [10] de Lima KPM, da Fonseca Dias V, da Silva JD. Numerical modelling for the solar driven bi-reforming of methane for the production of syngas in a solar thermochemical micro-packed bed reactor. *Int J Hydrogen Energy* 2020;45(17):10353–69. <http://dx.doi.org/10.1016/j.ijhydene.2019.08.241>, URL <https://www.sciencedirect.com/science/article/pii/S036031991933263X>. *AEM* 2018 - Smart Materials for Hydrogen Energy.
- [11] Shi X, Wang F, Cheng Z, Liang H, Dong Y, Chen X. Numerical analysis of the biomimetic leaf-type hierarchical porous structure to improve the energy storage efficiency of solar driven steam methane reforming. *Int J Hydrogen Energy* 2021;46(34):17653–65. <http://dx.doi.org/10.1016/j.ijhydene.2021.02.171>, URL <https://www.sciencedirect.com/science/article/pii/S036031992100745X>. Special issue on the 2nd International Symposium on Hydrogen Energy and Energy Technologies (HEET 2019).
- [12] Villafán-Vidales H, Abanades S, Caliot C, Romero-Paredes H. Heat transfer simulation in a thermochemical solar reactor based on a volumetric porous receiver. *Appl Therm Eng* 2011;31(16):3377–86. <http://dx.doi.org/10.1016/j.applthermaleng.2011.06.022>, URL <https://www.sciencedirect.com/science/article/pii/S1359431111003322>.
- [13] Ackermann S, Takacs M, Scheffe J, Steinfeld A. Reticulated porous ceria undergoing thermochemical reduction with high-flux irradiation. *Int J Heat Mass Transfer* 2017;107:439–49. <http://dx.doi.org/10.1016/j.ijheatmasstransfer.2016.11.032>, URL <https://www.sciencedirect.com/science/article/pii/S0017931016316003>.
- [14] Wang F, Shuai Y, Wang Z, Leng Y, Tan H. Thermal and chemical reaction performance analyses of steam methane reforming in porous media solar thermochemical reactor. *Int J Hydrogen Energy* 2014;39(2):718–30. <http://dx.doi.org/10.1016/j.ijhydene.2013.10.132>, URL <https://www.sciencedirect.com/science/article/pii/S0360319913026475>.
- [15] Chen X, Wang F, Han Y, Yu R, Cheng Z. Thermochemical storage analysis of the dry reforming of methane in foam solar reactor. *Energy Convers Manage* 2018;158:489–98. <http://dx.doi.org/10.1016/j.enconman.2017.12.066>, URL <https://www.sciencedirect.com/science/article/pii/S0196890417312189>.
- [16] Zhang H, Shuai Y, Lougou BG, Jiang B, Yang D, Pan Q, Wang F, Huang X. Effects of foam structure on thermochemical characteristics of porous-filled solar reactor. *Energy* 2022;239:122219. <http://dx.doi.org/10.1016/j.energy.2021.122219>, URL <https://www.sciencedirect.com/science/article/pii/S0360544221024671>.
- [17] Shi X, Shuai Y, Wang F, Zhang C, Cheng Z, Chen X. Effects of ordered hierarchically porous structure on methane reforming performance in solar foam reactor. *J CO₂ Util* 2020;37:147–57. <http://dx.doi.org/10.1016/j.jcou.2019.12.002>, URL <https://www.sciencedirect.com/science/article/pii/S2212982019310844>.
- [18] Hosseini F, Siavashi M. Optimization of SMR process for syngas production through a solar-assisted thermo-chemical reactor with a multi-layered porous core. *Sol Energy* 2021;230:208–21. <http://dx.doi.org/10.1016/j.solener.2021.10.026>, URL <https://www.sciencedirect.com/science/article/pii/S0038092X21008884>.
- [19] Wang F, Tan J, Ma L, Leng Y. Effects of key factors on solar aided methane steam reforming in porous medium thermochemical reactor. *Energy Convers Manage* 2015;103:419–30. <http://dx.doi.org/10.1016/j.enconman.2015.06.049>, URL <https://www.sciencedirect.com/science/article/pii/S0196890415005907>.
- [20] Wang F, Shuai Y, Tan H, Yu C. Thermal performance analysis of porous media receiver with concentrated solar irradiation. *Int J Heat Mass Transfer* 2013;62:247–54. <http://dx.doi.org/10.1016/j.ijheatmasstransfer.2013.03.003>, URL <https://www.sciencedirect.com/science/article/pii/S0017931013002081>.
- [21] Siavashi M, Hosseini F, Talesh Bahrami HR. A new design with preheating and layered porous ceramic for hydrogen production through methane steam reforming process. *Energy* 2021;231:120952. <http://dx.doi.org/10.1016/j.energy.2021.120952>, URL <https://www.sciencedirect.com/science/article/pii/S0360544221012007>.
- [22] Tang X-Y, Zhang K-R, Yang W-W, Dou P-Y. Integrated design of solar concentrator and thermochemical reactor guided by optimal solar radiation distribution. *Energy* 2023;263:125828. <http://dx.doi.org/10.1016/j.energy.2022.125828>, URL <https://www.sciencedirect.com/science/article/pii/S0360544222027141>.
- [23] Yang Y-J, Yang W-W, Ma X, Tang X-Y, Cao XE. Performance improvement of a solar volumetric reactor with passive thermal management under different solar radiation conditions. *Int J Hydrogen Energy* 2023. <http://dx.doi.org/10.1016/j.ijhydene.2023.02.102>, URL <https://www.sciencedirect.com/science/article/pii/S0360319923009588>.
- [24] Navalho JE, Pereira JC. A comprehensive and fully predictive discrete methodology for volumetric solar receivers: application to a functional parabolic dish solar collector system. *Appl Energy* 2020;267:114781. <http://dx.doi.org/10.1016/j.apenergy.2020.114781>, URL <https://www.sciencedirect.com/science/article/pii/S0360261920302932>.
- [25] Du S, Li M-J, Ren Q, Liang Q, He Y-L. Pore-scale numerical simulation of fully coupled heat transfer process in porous volumetric solar receiver. *Energy* 2017;140:1267–75. <http://dx.doi.org/10.1016/j.energy.2017.08.062>, URL <https://www.sciencedirect.com/science/article/pii/S0360544217314408>.
- [26] Du S, Tong Z-X, Zhang H-H, He Y-L. Tomography-based determination of nusselt number correlation for the porous volumetric solar receiver with different geometrical parameters. *Renew Energy* 2019;135:711–8. <http://dx.doi.org/10.1016/j.renene.2018.12.001>, URL <https://www.sciencedirect.com/science/article/pii/S0960148118314320>.
- [27] Moghimi H, Siavashi M, Mousavi Nezhad M, Guadagnini A. Pore-scale computational analyses of non-Darcy flow through highly porous structures with various degrees of geometrical complexity. *Sustain Energy Technol Assess* 2022;52:102048. <http://dx.doi.org/10.1016/j.seta.2022.102048>, URL <https://www.sciencedirect.com/science/article/pii/S221313882200100X>.
- [28] Sepehri E, Siavashi M. Pore-scale direct numerical simulation of fluid dynamics, conduction and convection heat transfer in open-cell Voronoi porous foams. *Int Commun Heat Mass Transfer* 2022;137:106274. <http://dx.doi.org/10.1016/j.icheatmasstransfer.2022.106274>, URL <https://www.sciencedirect.com/science/article/pii/S0735193322003967>.
- [29] Paknahad R, Siavashi M, Hosseini M. Pore-scale fluid flow and conjugate heat transfer study in high porosity Voronoi metal foams using multi-relaxation-time regularized lattice Boltzmann (MRT-RLB) method. *Int Commun Heat Mass Transfer* 2023;141:106607. <http://dx.doi.org/10.1016/j.icheatmasstransfer.2022.106607>, URL <https://www.sciencedirect.com/science/article/pii/S0735193322007291>.
- [30] Wang F, Tan J, Wang Z. Heat transfer analysis of porous media receiver with different transport and thermophysical models using mixture as feeding gas. *Energy Convers Manage* 2014;83:159–66. <http://dx.doi.org/10.1016/j.enconman.2014.03.068>, URL <https://www.sciencedirect.com/science/article/pii/S0196890414002696>.
- [31] Zhang H, Guene Lougou B, Pan R, Shuai Y, Wang F, Cheng Z, Tan H. Analysis of thermal transport and fluid flow in high-temperature porous media solar thermochemical reactor. *Sol Energy* 2018;173:814–24. <http://dx.doi.org/10.1016/j.solener.2018.08.015>, URL <https://www.sciencedirect.com/science/article/pii/S0038092X18307849>.
- [32] Lin Xia X, Chen X, Sun C, huan Li Z, Liu B. Experiment on the convective heat transfer from airflow to skeleton in open-cell porous foams. *Int J Heat Mass Transfer* 2017;106:83–90. <http://dx.doi.org/10.1016/j.ijheatmasstransfer.2016.10.053>, URL <https://www.sciencedirect.com/science/article/pii/S0017931016319214>.
- [33] Ni X, Liu T, Liu D. Effects of volumetric property models on the efficiency of a porous volumetric solar receiver. *Energies* 2022;15(11). <http://dx.doi.org/10.3390/en15113899>, URL <https://www.mdpi.com/1996-1073/15/11/3899>.
- [34] Kribus A, Gray Y, Grijnevich M, Mittelman G, Mey-Cloutier S, Caliot C. The promise and challenge of solar volumetric absorbers. *Sol Energy* 2014;110:463–81. <http://dx.doi.org/10.1016/j.solener.2014.09.035>, URL <https://www.sciencedirect.com/science/article/pii/S0038092X14004757>.
- [35] Mey S, Caliot C, Flamant G, Kribus A, Gray Y. Optimization of high temperature SiC volumetric solar absorber. *Energy Procedia* 2014;49:478–87. <http://dx.doi.org/10.1016/j.egypro.2014.03.051>, URL <https://www.sciencedirect.com/science/article/pii/S1876610214005050>. Proceedings of the SolarPACES 2013 International Conference.
- [36] Wang F, Tan J, Yong S, Tan H, Chu S. Thermal performance analyses of porous media solar receiver with different irradiative transfer models. *Int J Heat Mass Transfer* 2014;78:7–16. <http://dx.doi.org/10.1016/j.ijheatmasstransfer.2014.06.035>, URL <https://www.sciencedirect.com/science/article/pii/S0017931014005079>.

- [37] Zaversky F, Aldaz L, Sánchez M, Ávila-Marín AL, Roldán MI, Fernández-Reche J, Füssel A, Beckert W, Adler J. Numerical and experimental evaluation and optimization of ceramic foam as solar absorber – single-layer vs multi-layer configurations. *Appl Energy* 2018;210:351–75. <http://dx.doi.org/10.1016/j.apenergy.2017.11.003>, URL <https://www.sciencedirect.com/science/article/pii/S0306261917315787>.
- [38] Bai F. One dimensional thermal analysis of silicon carbide ceramic foam used for solar air receiver. *Int J Therm Sci* 2010;49(12):2400–4. <http://dx.doi.org/10.1016/j.ijthermalsci.2010.08.010>, URL <https://www.sciencedirect.com/science/article/pii/S129007291000236X>.
- [39] Wang P, Li J, Bai F, Liu D, Xu C, Zhao L, Wang Z. Experimental and theoretical evaluation on the thermal performance of a windowed volumetric solar receiver. *Energy* 2017;119:652–61. <http://dx.doi.org/10.1016/j.energy.2016.11.024>, URL <https://www.sciencedirect.com/science/article/pii/S0360544216316309>.
- [40] Xie T, Xu K-D, He Y-L, Wang K, Yang B-L. Thermodynamic and kinetic analysis of an integrated solar thermochemical energy storage system for dry-reforming of methane. *Energy* 2018;164:937–50. <http://dx.doi.org/10.1016/j.energy.2018.08.209>, URL <https://www.sciencedirect.com/science/article/pii/S0360544218317456>.
- [41] Cheng Z, He Y, Cui F. Numerical investigations on coupled heat transfer and synthetical performance of a pressurized volumetric receiver with MCRT-FVM method. *Appl Therm Eng* 2013;50(1):1044–54. <http://dx.doi.org/10.1016/j.applthermaleng.2012.08.045>, URL <https://www.sciencedirect.com/science/article/pii/S1359431112005777>.
- [42] Roldán M, Smirnova O, Fend T, Casas J, Zarza E. Thermal analysis and design of a volumetric solar absorber depending on the porosity. *Renew Energy* 2014;62:116–28. <http://dx.doi.org/10.1016/j.renene.2013.06.043>, URL <https://www.sciencedirect.com/science/article/pii/S0960148113003364>.
- [43] Godini A, Kheradmand S. Optimization of volumetric solar receiver geometry and porous media specifications. *Renew Energy* 2021;172:574–81. <http://dx.doi.org/10.1016/j.renene.2021.03.040>, URL <https://www.sciencedirect.com/science/article/pii/S0960148121003943>.
- [44] Gu R, Ding J, Wang Y, Yuan Q, Wang W, Lu J. Heat transfer and storage performance of steam methane reforming in tubular reactor with focused solar simulator. *Appl Energy* 2019;233–234:789–801. <http://dx.doi.org/10.1016/j.apenergy.2018.10.072>, URL <https://www.sciencedirect.com/science/article/pii/S0306261918316404>.
- [45] Wu Z, Caliot C, Flamant G, Wang Z. Coupled radiation and flow modeling in ceramic foam volumetric solar air receivers. *Sol Energy* 2011;85(9):2374–85. <http://dx.doi.org/10.1016/j.solener.2011.06.030>, URL <https://www.sciencedirect.com/science/article/pii/S0038092X11002428>.
- [46] Xu C, Song Z, der Chen L, Zhen Y. Numerical investigation on porous media heat transfer in a solar tower receiver. *Renew Energy* 2011;36(3):1138–44. <http://dx.doi.org/10.1016/j.renene.2010.09.017>, URL <https://www.sciencedirect.com/science/article/pii/S0960148110004489>.
- [47] Chen X, Xia X-L, Liu H, Li Y, Liu B. Heat transfer analysis of a volumetric solar receiver by coupling the solar radiation transport and internal heat transfer. *Energy Convers Manage* 2016;114:20–7. <http://dx.doi.org/10.1016/j.enconman.2016.01.074>, URL <https://www.sciencedirect.com/science/article/pii/S019689041630022X>.
- [48] Chen X, Wang F, Yan X, Han Y, Cheng Z, Jie Z. Thermochemical performance of solar driven CO₂ reforming of methane in volumetric reactor with gradual foam structure. *Energy* 2018;151:545–55. <http://dx.doi.org/10.1016/j.energy.2018.03.086>, URL <https://www.sciencedirect.com/science/article/pii/S036054421830495X>.
- [49] Barreto G, Canhoto P, Collares-Pereira M. Three-dimensional CFD modelling and thermal performance analysis of porous volumetric receivers coupled to solar concentration systems. *Appl Energy* 2019;252:113433. <http://dx.doi.org/10.1016/j.apenergy.2019.113433>, URL <https://www.sciencedirect.com/science/article/pii/S0360261919311079>.
- [50] Salomons S, Hayes R, Poirier M, Sapoundjiev H. Modelling a reverse flow reactor for the catalytic combustion of fugitive methane emissions. *Comput Chem Eng* 2004;28(9):1599–610. <http://dx.doi.org/10.1016/j.compchemeng.2003.12.006>, URL <https://www.sciencedirect.com/science/article/pii/S009813540300317X>.
- [51] Kim Y-D, Jeong S-J, Kim W-S. Optimal design of axial noble metal distribution for improving dual monolithic catalytic converter performance. *Chem Eng Sci* 2009;64(7):1373–83. <http://dx.doi.org/10.1016/j.ces.2008.11.020>, URL <https://www.sciencedirect.com/science/article/pii/S0009250908006416>.
- [52] Maestri M, Cuoci A. Coupling CFD with detailed microkinetic modeling in heterogeneous catalysis. *Chem Eng Sci* 2013;96:106–17. <http://dx.doi.org/10.1016/j.ces.2013.03.048>, URL <https://www.sciencedirect.com/science/article/pii/S0009250913002327>.
- [53] Navalho JE, Pereira JM, Pereira JC. Conical-shaped foam reactors for catalytic partial oxidation applications. *Int J Hydrogen Energy* 2014;39(8):3666–80. <http://dx.doi.org/10.1016/j.ijhydene.2013.12.107>, URL <https://www.sciencedirect.com/science/article/pii/S0360319913030711>.
- [54] Koltsakis GC, Stamatelos AM. Catalytic automotive exhaust aftertreatment. *Prog Energy Combust Sci* 1997;23(1):1–39. [http://dx.doi.org/10.1016/S0360-1285\(97\)00003-8](http://dx.doi.org/10.1016/S0360-1285(97)00003-8), URL <https://www.sciencedirect.com/science/article/pii/S0360128597000038>.
- [55] Hayes R, Kolaczowski S. Introduction to catalytic combustion. Gordon and Breach Science Publishers; 1997.
- [56] Maestri M, Beretta A, Groppi G, Tronconi E, Forzatti P. Comparison among structured and packed-bed reactors for the catalytic partial oxidation of CH₄ at short contact times. *Catal Today* 2005;105(3):709–17. <http://dx.doi.org/10.1016/j.cattod.2005.06.045>, URL <https://www.sciencedirect.com/science/article/pii/S092058610500266X>. 2nd International Conference on Structured Catalysts and Reactors ICOSCAR-2.
- [57] Scognamiglio D, Russo L, Maffettone PL, Saleme L, Simeone M, Crescitelli S. Modelling and simulation of a catalytic autothermal methane reformer with Rh catalyst. *Int J Hydrogen Energy* 2012;37(1):263–75. <http://dx.doi.org/10.1016/j.ijhydene.2011.08.092>, URL <https://www.sciencedirect.com/science/article/pii/S0360319911020167>. 11th China Hydrogen Energy Conference.
- [58] Chatterjee D, Schmeißer V, Frey M, Weibel M. Perspectives of the automotive industry on the modeling of exhaust gas aftertreatment catalysts. John Wiley & Sons, Ltd; 2011, p. 303–43. <http://dx.doi.org/10.1002/9783527639878.ch10>, Ch. 10. [arXiv:https://onlinelibrary.wiley.com/doi/pdf/10.1002/9783527639878.ch10](https://onlinelibrary.wiley.com/doi/pdf/10.1002/9783527639878.ch10). URL <https://onlinelibrary.wiley.com/doi/abs/10.1002/9783527639878.ch10>.
- [59] Depcik C, Assanis D. One-dimensional automotive catalyst modeling. *Prog Energy Combust Sci* 2005;31(4):308–69. <http://dx.doi.org/10.1016/j.pecs.2005.08.001>, URL <https://www.sciencedirect.com/science/article/pii/S0360128505000237>.
- [60] Wang F, Tan J, Shuai Y, Gong L, Tan H. Numerical analysis of hydrogen production via methane steam reforming in porous media solar thermochemical reactor using concentrated solar irradiation as heat source. *Energy Convers Manage* 2014;87:956–64. <http://dx.doi.org/10.1016/j.enconman.2014.08.003>, URL <https://www.sciencedirect.com/science/article/pii/S0196890414007274>.
- [61] Fuqiang W, Jianyu T, Huijian J, Yu L. Thermochemical performance analysis of solar driven CO₂ methane reforming. *Energy* 2015;91:645–54. <http://dx.doi.org/10.1016/j.energy.2015.08.080>, URL <https://www.sciencedirect.com/science/article/pii/S0360544215011561>.
- [62] Shi X, Wang F, Lougou BG, Zhang H, Wei X, Li D, Xu J. Experimental and numerical study regarding the biomimetic bone porous structure to match energy and mass flow in a solar thermochemical reactor. *J Energy Storage* 2022;55:105645. <http://dx.doi.org/10.1016/j.est.2022.105645>, URL <https://www.sciencedirect.com/science/article/pii/S2352152X22016334>.
- [63] Edouard D, Lacroix M, Pham C, Mbodji M, Pham-Huu C. Experimental measurements and multiphase flow models in solid SiC foam beds. *AIChE J* 2008;54(11):2823–32. <http://dx.doi.org/10.1002/aic.11594>, [arXiv:https://aiche.onlinelibrary.wiley.com/doi/pdf/10.1002/aic.11594](https://aiche.onlinelibrary.wiley.com/doi/pdf/10.1002/aic.11594). URL <https://aiche.onlinelibrary.wiley.com/doi/abs/10.1002/aic.11594>.
- [64] Schwiedernoch R, Tischer S, Correa C, Deuschmann O. Experimental and numerical study on the transient behavior of partial oxidation of methane in a catalytic monolith. *Chem Eng Sci* 2003;58(3):633–42. [http://dx.doi.org/10.1016/S0009-2509\(02\)00589-4](http://dx.doi.org/10.1016/S0009-2509(02)00589-4), URL <https://www.sciencedirect.com/science/article/pii/S0009250902005894>. 17th International Symposium of Chemical Reaction Engineering (IS CRE 17).
- [65] Beretta A, Donazzi A, Livio D, Maestri M, Groppi G, Tronconi E, Forzatti P. Optimal design of a CH₄ CPO-reformer with honeycomb catalyst: Combined effect of catalyst load and channel size on the surface temperature profile. *Catal Today* 2011;171(1):79–83. <http://dx.doi.org/10.1016/j.cattod.2011.03.081>, URL <https://www.sciencedirect.com/science/article/pii/S0920586111003981>.
- [66] Deuschmann O. Catalytic reforming of logistic fuels at high-temperatures. In: *Catalysis*. The Royal Society of Chemistry; 2012, <http://dx.doi.org/10.1039/9781849734776-00048>.
- [67] Chen J, Gao X, Yan L, Xu D. Millisecond methane steam reforming for hydrogen production: A computational fluid dynamics study. *Int J Hydrogen Energy* 2018;43(29):12948–69. <http://dx.doi.org/10.1016/j.ijhydene.2018.05.039>, URL <https://www.sciencedirect.com/science/article/pii/S0360319918315295>.
- [68] Shi X, Xun Y, Dong Y, Wang F, Zhang X, Cheng Z. Analysis of biomimetic hierarchical porous structure regulating radiation field to improve solar thermochemical performance based on minimum Gibbs free energy. *Int J Hydrogen Energy* 2022;47(5):2832–45. <http://dx.doi.org/10.1016/j.ijhydene.2021.10.246>, URL <https://www.sciencedirect.com/science/article/pii/S0360319921043561>. Hydrogen Energy and Fuel Cells.
- [69] Kee RJ, Coltrin ME, Glarborg P. *Chemically reacting flow: theory and practice*. John Wiley & Sons; 2003.
- [70] Poinot T, Veynante D. *Theoretical and numerical combustion*. RT Edwards, Inc.; 2005.
- [71] Wheeler VM, Bader R, Kreider PB, Hangi M, Haussener S, Lipiński W. Modelling of solar thermochemical reaction systems. *Sol Energy* 2017;156:149–68. <http://dx.doi.org/10.1016/j.solener.2017.07.069>, URL <https://www.sciencedirect.com/science/article/pii/S0038092X17306552>. *Advances in Solar Thermochemistry*.

- [72] Groppi G, Tronconi E, Forzatti P. Mathematical models of catalytic combustors. *Catal Rev* 1999;41(2):227–54. <http://dx.doi.org/10.1080/01614949909353780>, arXiv:<https://doi.org/10.1080/01614949909353780>.
- [73] Chen J, Yang H, Wang N, Ring Z, Dabros T. Mathematical modeling of monolith catalysts and reactors for gas phase reactions. *Appl Catal A: Gener* 2008;345(1):1–11. <http://dx.doi.org/10.1016/j.apcata.2008.04.010>, URL <https://www.sciencedirect.com/science/article/pii/S0926860X08002251>.
- [74] Navalho JE, Pereira JM, Ervilha AR, Pereira JC. Uncertainty quantification in the catalytic partial oxidation of methane. *Combust Theory Model* 2013;17(6):1067–95. <http://dx.doi.org/10.1080/13647830.2013.826823>, arXiv:<https://doi.org/10.1080/13647830.2013.826823>.
- [75] Navalho JEP, Pereira JMC, Pereira JCF. Multiscale modeling of methane catalytic partial oxidation: From the mesopore to the full-scale reactor operation. *AIChE J* 2018;64(2):578–94. <http://dx.doi.org/10.1002/aic.15945>, arXiv:<https://aiche.onlinelibrary.wiley.com/doi/pdf/10.1002/aic.15945>. URL <https://aiche.onlinelibrary.wiley.com/doi/abs/10.1002/aic.15945>.
- [76] Zhu H, Kee RJ, Engel JR, Wickham DT. Catalytic partial oxidation of methane using RhSr- and Ni-substituted hexaaluminates. *Proc Combust Inst* 2007;31(2):1965–72. <http://dx.doi.org/10.1016/j.proci.2006.07.028>, URL <https://www.sciencedirect.com/science/article/pii/S1540748906000356>.
- [77] Murphy DM, Richards AE, Colclasure AM, Rosensteel W, Sullivan N. Biogas fuel reforming for solid oxide fuel cells. *ECS Trans* 2011;35(1):2653. <http://dx.doi.org/10.1149/1.3570265>.
- [78] Al-Matouq A, Vincent T. On-line estimation of inlet and outlet composition in catalytic partial oxidation. *Int J Hydrogen Energy* 2014;39(13):6953–66. <http://dx.doi.org/10.1016/j.ijhydene.2014.02.049>, URL <https://www.sciencedirect.com/science/article/pii/S0360319914004091>.
- [79] Lemlich R. A theory for the limiting conductivity of polyhedral foam at low density. *J Colloid Interface Sci* 1978;64(1):107–10. [http://dx.doi.org/10.1016/0021-9797\(78\)90339-9](http://dx.doi.org/10.1016/0021-9797(78)90339-9), URL <http://www.sciencedirect.com/science/article/pii/0021979778903399>.
- [80] Schuetz M, Glicksman L. A basic study of heat transfer through foam insulation. *J Cell Plast* 1984;20(2):114–21.
- [81] Du S, He Y-L, Yang W-W, Liu Z-B. Optimization method for the porous volumetric solar receiver coupling genetic algorithm and heat transfer analysis. *Int J Heat Mass Transfer* 2018;122:383–90. <http://dx.doi.org/10.1016/j.ijheatmasstransfer.2018.01.120>, URL <https://www.sciencedirect.com/science/article/pii/S0017931017347853>.
- [82] Du S, Xia T, He Y-L, Li Z-Y, Li D, Xie X-Q. Experiment and optimization study on the radial graded porous volumetric solar receiver matching non-uniform solar flux distribution. *Appl Energy* 2020;275:115343. <http://dx.doi.org/10.1016/j.apenergy.2020.115343>, URL <https://www.sciencedirect.com/science/article/pii/S0306261920308552>.
- [83] Lee H-J, Kim J-K, Lee S-N, Kang Y-H. Consistent heat transfer analysis for performance evaluation of multichannel solar absorbers. *Sol Energy* 2012;86(5):1576–85. <http://dx.doi.org/10.1016/j.solener.2012.02.020>, URL <https://www.sciencedirect.com/science/article/pii/S0038092X12000849>.
- [84] Jung EG, Boo JH, Kang YH, Kim NH. Effectiveness of a multi-channel volumetric air receiver for a solar power tower. *Heat Mass Transf* 2013;49(8):1181–90. <http://dx.doi.org/10.1007/s00231-013-1164-5>.
- [85] Kasaean A, Barghamadi H, Pourfayaz F. Performance comparison between the geometry models of multi-channel absorbers in solar volumetric receivers. *Renew Energy* 2017;105:1–12. <http://dx.doi.org/10.1016/j.renene.2016.12.038>, URL <https://www.sciencedirect.com/science/article/pii/S0960148116310941>.
- [86] Zhu Q, Xuan Y. Pore scale numerical simulation of heat transfer and flow in porous volumetric solar receivers. *Appl Therm Eng* 2017;120:150–9. <http://dx.doi.org/10.1016/j.applthermaleng.2017.03.141>, URL <https://www.sciencedirect.com/science/article/pii/S1359431116324590>.
- [87] Heterogeneous chemistry. John Wiley & Sons, Ltd; 2003, p. 445–86. <http://dx.doi.org/10.1002/0471461296.ch11>, arXiv:<https://onlinelibrary.wiley.com/doi/pdf/10.1002/0471461296.ch11>. URL <https://onlinelibrary.wiley.com/doi/abs/10.1002/0471461296.ch11>.
- [88] Kunz L, Maier L, Tischer S, Deutschmann O. Modeling the Rate of Heterogeneous Reactions. John Wiley & Sons, Ltd; 2011, p. 113–48. <http://dx.doi.org/10.1002/9783527639878.ch4>, Ch. 4. arXiv:<https://onlinelibrary.wiley.com/doi/pdf/10.1002/9783527639878.ch4>. URL <https://onlinelibrary.wiley.com/doi/abs/10.1002/9783527639878.ch4>.
- [89] Karakaya C, Maier L, Deutschmann O. Surface reaction kinetics of the oxidation and reforming of CH₄ over Rh/Al₂O₃ catalysts. *Int J Chem Kinet* 2016;48(3):144–60. <http://dx.doi.org/10.1002/kin.20980>, arXiv:<https://onlinelibrary.wiley.com/doi/pdf/10.1002/kin.20980>. URL <https://onlinelibrary.wiley.com/doi/abs/10.1002/kin.20980>.
- [90] Smith GP, Golden DM, Frenklach M, Moriarty NW, Eiteneer B, Goldenberg M, Bowman CT, Hanson RK, Song S, Gardiner Jr WC, Lissianski VV, Qin Z. GRI-mech 3.0, 1999. 1999, URL http://www.me.berkeley.edu/gri_mech.
- [91] Chen X, Xia X-L, Yan X-W, Sun C. Heat transfer analysis of a volumetric solar receiver with composite porous structure. *Energy Convers Manage* 2017;136:262–9. <http://dx.doi.org/10.1016/j.enconman.2017.01.018>, URL <https://www.sciencedirect.com/science/article/pii/S0196890417300183>.
- [92] feng Hsu P, Howell JR. Measurements of thermal conductivity and optical properties of porous partially stabilized zirconia. *Exp Heat Transfer* 1992;5(4):293–313. <http://dx.doi.org/10.1080/08916159208946446>, arXiv:<https://doi.org/10.1080/08916159208946446>.
- [93] Vafai K. *Handbook of porous media*. CRC Press; 2005.
- [94] Nimvari ME, Jouybari NF, Esmaili Q. A new approach to mitigate intense temperature gradients in ceramic foam solar receivers. *Renew Energy* 2018;122:206–15. <http://dx.doi.org/10.1016/j.renene.2018.01.117>, URL <https://www.sciencedirect.com/science/article/pii/S0960148118301277>.
- [95] Sharma S, Talukdar P. Thermo-mechanical analysis of a porous volumetric solar receiver subjected to concentrated solar radiation. *Sol Energy* 2022;247:41–54. <http://dx.doi.org/10.1016/j.solener.2022.10.014>, URL <https://www.sciencedirect.com/science/article/pii/S0038092X22007472>.
- [96] Goodwin D. An open-source, extensible software suite for CFD process simulation. *Chem Vapor Depos XVI EUROCV D* 2003;14(40):2003–8.
- [97] Talukdar P, Mishra SC. Analysis of conduction–radiation problem in absorbing, emitting and anisotropically scattering media using the collapsed dimension method. *Int J Heat Mass Transfer* 2002;45(10):2159–68. [http://dx.doi.org/10.1016/S0017-9310\(01\)00305-2](http://dx.doi.org/10.1016/S0017-9310(01)00305-2), URL <https://www.sciencedirect.com/science/article/pii/S0017931001003052>.
- [98] Dalle Nogare D, Degenstein N, Horn R, Canu P, Schmidt L. Modeling spatially resolved profiles of methane partial oxidation on a rh foam catalyst with detailed chemistry. *J Catal* 2008;258(1):131–42. <http://dx.doi.org/10.1016/j.jcat.2008.06.006>, URL <https://www.sciencedirect.com/science/article/pii/S0021951708002182>.
- [99] Zhu Q, Xuan Y. Performance analysis of a volumetric receiver composed of packed shaped particles with spectrally dependent emissivity. *Int J Heat Mass Transfer* 2018;122:421–31. <http://dx.doi.org/10.1016/j.ijheatmasstransfer.2018.02.006>, URL <https://www.sciencedirect.com/science/article/pii/S0017931017344320>.
- [100] Navalho J, Frenzel I, Loukou A, Pereira J, Trimis D, Pereira J. Catalytic partial oxidation of methane rich mixtures in non-adiabatic monolith reactors. *Int J Hydrogen Energy* 2013;38(17):6989–7006. <http://dx.doi.org/10.1016/j.ijhydene.2013.02.141>, URL <https://www.sciencedirect.com/science/article/pii/S0360319913006502>.
- [101] Wu Z, Caliot C, Flamant G, Wang Z. Numerical simulation of convective heat transfer between air flow and ceramic foams to optimise volumetric solar air receiver performances. *Int J Heat Mass Transfer* 2011;54(7):1527–37. <http://dx.doi.org/10.1016/j.ijheatmasstransfer.2010.11.037>, URL <https://www.sciencedirect.com/science/article/pii/S0017931010006514>.
- [102] Teng L, Xuan Y. Thermal and hydrodynamic performance of a novel volumetric solar receiver. *Sol Energy* 2018;163:177–88. <http://dx.doi.org/10.1016/j.solener.2018.01.087>, URL <https://www.sciencedirect.com/science/article/pii/S0038092X18301087>.
- [103] Andreozzi A, Bianco N, Iasiello M, Naso V. Thermo-fluid-dynamics of a ceramic foam solar receiver: A parametric analysis. *Heat Transf Eng* 2020;41(12):1085–99. <http://dx.doi.org/10.1080/01457632.2019.1600876>, arXiv:<https://doi.org/10.1080/01457632.2019.1600876>.
- [104] Li X-L, Xia X-L, Sun C, Chen Z-H. Performance analysis on a volumetric solar receiver with an annular inner window. *Renew Energy* 2021;170:487–99. <http://dx.doi.org/10.1016/j.renene.2021.01.141>, URL <https://www.sciencedirect.com/science/article/pii/S0960148121001543>.
- [105] Ren Y, Qi H, Shi J, Chen Q, Wang Y, Ruan L. Thermal performance characteristics of porous media receiver exposed to concentrated solar radiation. *J Energy Eng* 2017;143(5):04017013. [http://dx.doi.org/10.1061/\(ASCE\)EY.1943-7897.0000448](http://dx.doi.org/10.1061/(ASCE)EY.1943-7897.0000448), arXiv:<https://ascelibrary.org/doi/pdf/10.1061/%28ASCE%29EY.1943-7897.0000448>. URL <https://ascelibrary.org/doi/abs/10.1061/%28ASCE%29EY.1943-7897.0000448>.
- [106] Reddy K, Nataraj S. Thermal analysis of porous volumetric receivers of concentrated solar dish and tower systems. *Renew Energy* 2019;132:786–97. <http://dx.doi.org/10.1016/j.renene.2018.08.030>, URL <https://www.sciencedirect.com/science/article/pii/S0960148118309807>.